Validation of Aeolus wind and aerosol products with ground-based and shipborne measurements

MASTER THESIS

submitted to

the Faculty of Physics and Earth Science
of Leipzig University

to award the academic degree

Master of Science

handed in by

B.Sc. Alina Herzog

Reviewer: Prof. Dr. Andreas Macke
Leibniz Institute for Tropospheric Research
Prof. Dr. Johannes Quaas
Leipzig Institute for Meteorology
Advisor: Dr. Birgit Heese
Dr. Holger Baars

Leipzig
October 24, 2019

Abstract

In August 2018 the satellite Aeolus with the worldwide first Doppler wind lidar in space on board was launched. By performing global horizontal wind measurements on molecules and particles in vertical ranges between 0 km to 30 km it is a promising new technology to improve the quality of weather forecasts and the understanding of the atmospheric processes. To quantify the quality, validations and calibrations with weather models and with measurements of radiosondes, balloons, satellites, aircraft, and ground-based instruments are necessary. In this thesis unique shipborne validation across the Atlantic Ocean and land-based validation in Leipzig are performed and analysed, using radiosondes and Polly^{XT} lidars. The validations show the success of the Aeolus mission, having correlations up to 92.8 % between Aeolus and radiosonde measurements. Furthermore, reasons of measurement deviations in the validations are discussed as well as the current challenges of the Aeolus mission.

Zusammenfassung

Im August 2018 wurde der Satellit Aeolus erfolgreich mit dem ersten Doppler Windlidar an Bord auf seine Umlaufbahn gebracht. Mit der Möglichkeit global horizontalen Wind an Molekülen und Partikeln in Höhen bis zu 30 km zu messen, verfügt der Satellit eine vielversprechende Technologie um Wettervorhersagen zu verbessern und das Verständnis der atmosphärischen Prozesse zu erweitern. Um seine Qualität zu überprüfen, sind Validierungen und Kalibrierungen mit Wettermodellen und mit Messungen von Radiosonden, Ballonen, Satelliten, sowie flugzeuggebundenen und bodenbasierten Messgeräten notwendig. In dieser Arbeit werden einzigartige schiffsgebundenen und bodenbasierte Validierungen mit Radiosonden und Polly^{XT} Lidars über dem Atlantischen Ozean, sowie in Leipzig durchgeführt. Sie zeigen den Erfolg der Aeolusmission, mit Korrelationen zwischen Aeolus- und Radiosondenmessungen bis zu 92.8 %. Desweiteren werden die Gründe für Abweichungen in diesen Validierungen und die momentanen Herausforderungen der Aeolus Mission diskutiert.

Contents

1 Introduction

On 22 August 2018 the new satellite Atmospheric Dynamics Mission (ADM) Aeolus was successfully launched. Aeolus belongs to the European Space Agency (ESA) Earth Explorer Core Mission and has the worldwide first Doppler wind lidar in space on board (lidar: **l**ight **d**etection **a**nd **r**anging), called Atmospheric Laser Doppler Instrument (ALADIN). Its mission is to demonstrate the new technology for horizontal wind measurements from space in order to improve the quality of weather forecasts and to advance the understanding of atmospheric dynamics and climate processes [1].

For precise weather forecast the Numerical Weather Prediction (NWP) models rely on the data assimilation of worldwide meteorological observations. But as shown in Figure 1.1 the global observation system lacks in an even in situ wind observation distribution. The Figure shows the global (a) and vertical (b) direct wind observing system that is assimilated at the European Centre of Medium-Range Weather Forecasts (ECMWF) model from late 2016 [2]. The observations are mainly made by aircraft, radiosondes, and Atmospheric Motion Vectors (AMV). AMV describe the method of observing the movement of objects (like clouds) from space and deriving the wind velocity from its movement. But as the AMV method provides only wind information in the troposphere and there are only few aircraft and radiosonde measurements in the lower stratosphere, the coverage in the lower stratosphere is poor. Furthermore, the main input of aircraft measurements is in Europe and the USA and not globally distributed. Therefore the observations are suffering from a shortage, especially on the Southern Hemisphere, in the lower stratosphere and over the Oceans.

The aim of Aeolus is to fill these gaps by providing global horizontal wind profiles in altitudes from 0 km to 30 km, ready for data assimilation in NWP models.

Within the German initiative *Experimental Validation and Assimilation of Aeolus observations* (EVAA) experimental validation for Aeolus are conducted by the *Meteorological Institute of the Ludwig Maximilian University of Munich* (MIM), *Leibniz Institute for Tropospheric Research* (TROPOS), *Deutscher Wetterdienst* (DWD), and the *Deutsche Luft- und Raumfahrt* (DLR). As part of these activities, the regular participation of TROPOS on Polarstern cruises within the OCEANET project [3, 4, 5, 6] offered the opportunity to perform ground-based validation above the Atlantic Ocean. With no ground station on the Atlantic Ocean, this was an unique chance to achieve ground-based measurements in this area. The cruise PS116

(a) Global wind observation distribution **(b)** Vertical wind observation distribution

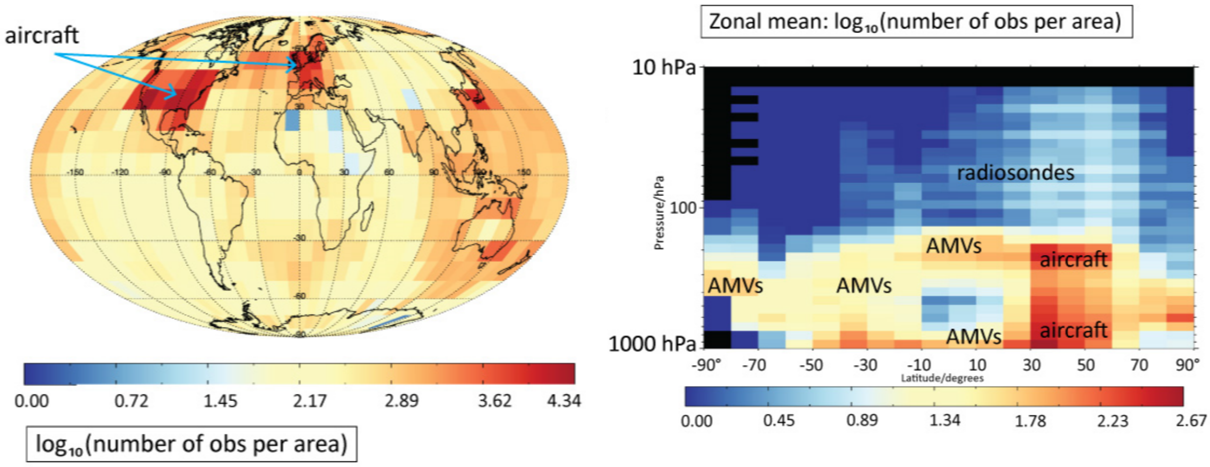

Figure 1.1: The global (a) and vertical (b) distribution of the direct wind observations that are assimilated at the ECMWF from late 2016 [2].

from Bremerhaven to Cape Town took place from 10 November 2018 to 11 December 2018 [7]. Starting in the Northern mid-latitudes and ending in the Southern subtropical region at a latitude of -33.92°, Polarstern passed various wind pattern, typical for the different latitudes along the cruise. Figure 1.2 illustrates the most important global circulation systems and wind flows, including the Polar cell, Ferrel cell, the Hadley cell, and the Polar and Subtropical jet stream [8]. Polarstern started in the Northern mid-latitude region, which has frequently westerly winds at ground level. It passed the region of the Subtropical jet stream and continued towards the North-East and South-East trade winds in the tropics, crossing the Inter-Tropical Convergence Zone (ITCZ) and finally ended up in the subtropical region in Cape Town.
The validation could be realised with the OCEANET facility of TROPOS, including the portable multiwavelength Raman polarization lidar, called *Polly*^{XT} [10] and additional radiosondes, provided by the DWD on Polarstern [11].

This thesis will provide an overview and the challenges of the Aeolus mission, the principle of the Doppler wind lidar and ALADINs instrumental setup. Furthermore, case studies and statistics of the shipborne validation for wind and aerosol measurements as well as land-based wind validation, taken place in Leipzig, are compared to the measurements of Aeolus and will be analysed and discussed.

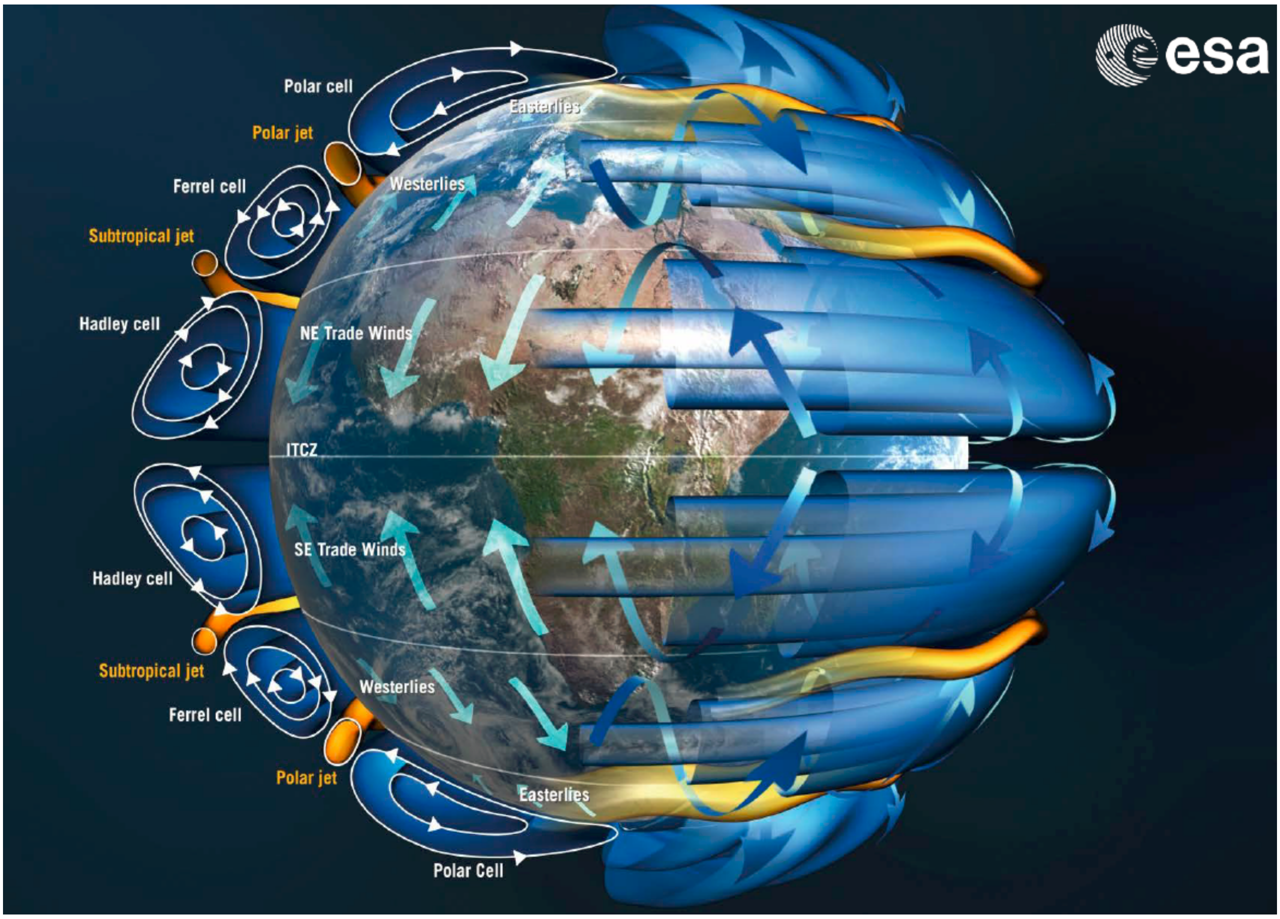

Figure 1.2: A sketch of the atmospheric wind circulation, illustrating the most important global circulation systems, wind flows and jet streams [9].

2 Overview of Aeolus

This chapter provides an overview of the most important key points of Aeolus, including the basic concept, the sampling terminology and the ideal mission requirements.

In 1999 ESA chose the ADM wind lidar as the 2nd Earth Explorer Core mission. The name Aeolus was inspired by the keeper of the wind in Greek mythology [12]. ALADIN, the instrument on board, is a High Spectral Resolution (HSR) elastic backscatter lidar with a Nd-YAG laser operating at a wavelength of 355 nm. The laser pulses are emitted with a frequency of 50.5 Hz and a circular polarization. The wind profiles are obtained from laser light, that is backscattered at moving air molecules and particles. The signals are separately detected by two different receiver channels, the Rayleigh channel for molecular and the Mie channel for particle backscatter. This has the advantage of two independent wind measurements. Furthermore, it gives the possibility to subsequently perform aerosol measurements, providing the particle extinction and the particle backscatter coefficient independently [13].

The basic concept of Aeolus is shown in Figure 2.1. It has a weekly repeating polar, sun-synchronous orbit with an inclination of 97° and a mean altitude of 320 km. One orbit period has a duration of 90.8 minutes and a ground track velocity of about 7200 ms^{-1}. The line-of-sight (LOS) describes the field of view in which the backscattered light from the emitted laser pulses can be collected by the lidar. It has an angle of 35° versus nadir, to be able to measure the horizontal line-of-sight (HLOS) wind velocity. It should be mentioned that this angle changes to 37.6° on the measurement ground point due to the earth curvature [14].

Besides in strong convection cases, the vertical wind velocity is small compared to the horizontal wind, thus the vertical component can be neglected. Furthermore, the LOS is orthogonal to the flight direction to minimize the effect of the satellite velocity on the wind measurements. The orbit is aligned such that Aeolus flies along the day/night border facing towards the night side to minimize the solar background radiation. Thus, the overpasses are either in the morning (descending orbit) at around 6 am or in the evening (ascending orbit) at around 6 pm local time. Passing from North to South in the morning, Aeolus's viewing direction has an azimuth angle of around 100°. This leads to a main measurement of the horizontal west/east wind component, having a positive sign of east winds along the LOS. Consequently the sign is vice versa for the Aeolus track from South to North, having an azimuth angle of around 260°.

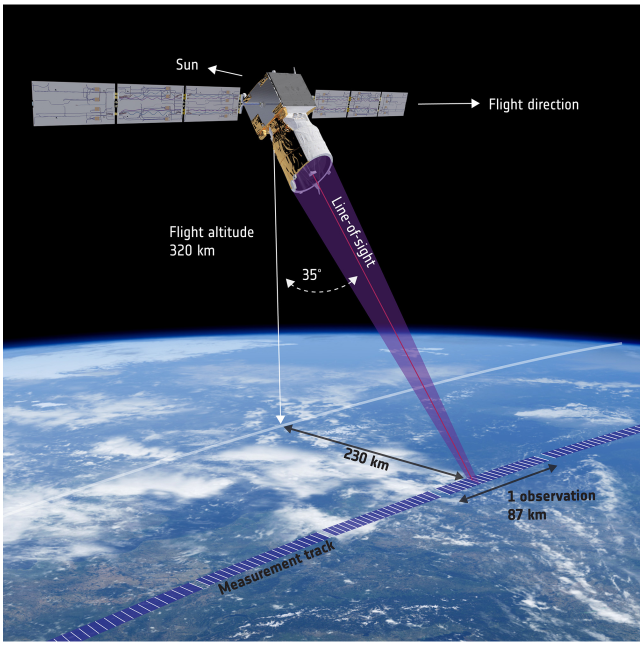

Figure 2.1: Basis concept of the Aeolus satellite. The line-of-sight indicates the field of view of the received backscattered signals from the emitted laser pulses [14].

The sampling terminology of the HLOS wind profiles is shown in Figure 2.2. The accumulation of 19 outgoing laser pulses on the instrument is called one **measurement** and corresponds to a horizontal length of around ≈ 3 km. One **observation** is the averaging of several measurements. The number of measurements included in one observation can be modified, depended on the integration length that is wanted. In the output product, the observation is included as one wind or aerosol profile, having the integration length as horizontal resolution. Each profile is subdivided in 24 vertical layers between 0 m to 30 km with a vertical resolution between 250 m to 2 km [14].

The most important ideal observational mission requirements of the ADM-Aeolus Mission are listed in Table 2.1. The vertical resolution shall achieve 500 m in the Planetary Boundary Layer (PBL), 1 km in the troposphere and 2 km in the lower stratosphere. The requirements for the horizontal integration length per observation depends on the measurement product and altitude. 90 km is required for the preliminary HLOS wind (called Level 1B product and will be described later on), 100 km is used for the wind accuracy requirement below and 140 km above an altitude of 14 km [14]. The precision of the HLOS component shall be 1 ms^{-1} for the PBL, 2.5 ms^{-1} for the troposphere and 3 ms^{-1} for the lower stratosphere. As the measurement shall improve the weather forecast by data assimilation, the data must be available within 3 hours [14].

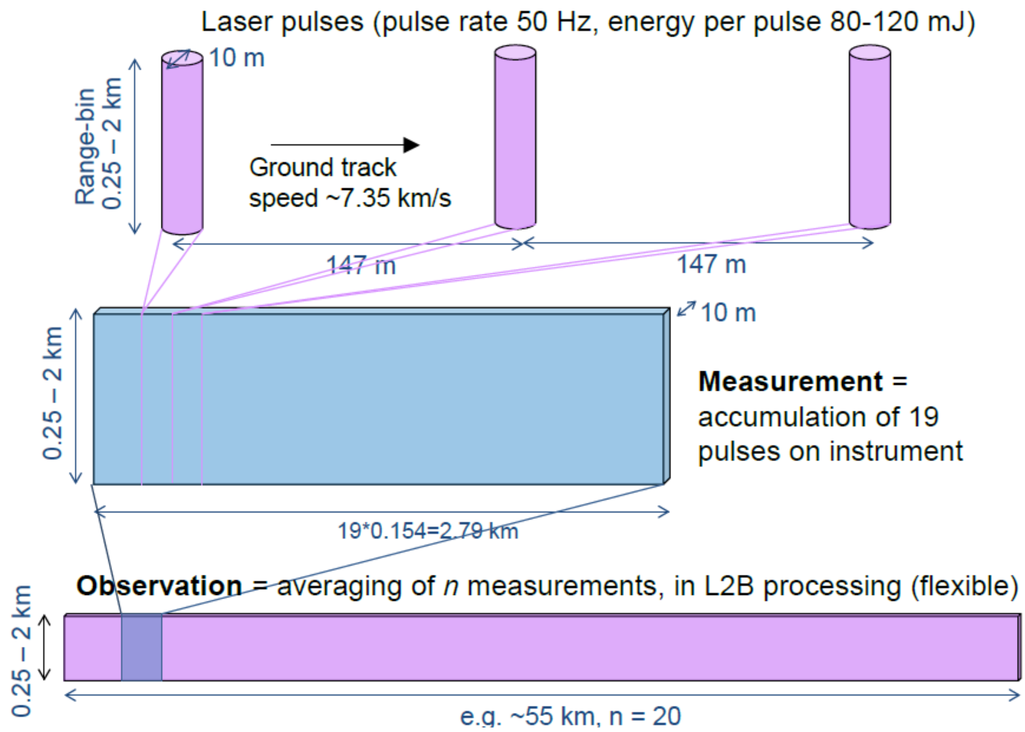

Figure 2.2: The Aeolus sampling terminology. The distance lengths differ as the ground track velocity has changed due to a different flight altitude of the satellite [15].

Parameter	**Planetary Boundary Layer**	**Troposphere**	**Stratosphere**
vertical domain	0-2 km	2-16 km	16-20 km
vertical resolution	0.5 km	1 km	2 km
horizontal integration length per observation	90/100/140 km		
precision HLOS component	1 ms^{-1}	2.5 ms^{-1}	3 ms^{-1}
data availability, timeliness	3 hours		

Table 2.1: The most important ideal mission requirements of the ADM Aeolus mission [14].

3 Doppler Wind Lidar ALADIN

In this chapter the principle of a lidar will be explained. It focuses on the function of the Doppler wind lidar ALADIN, including the measurement principle of a Doppler lidar and the optical architecture of ALADIN. Furthermore, a simulation example of the Aeolus wind profiles is shown and the aerosol and cloud property measurements are discussed.

3.1 Lidar principle

The acronym LIDAR was first introduced by Middleton and Spilhaus in 1953 [16] and is nowadays used as an own word, written as lidar. It is used as an active remote sensing system. Its basic components are shown in Figure 3.1, in this case for the space lidar ALADIN.

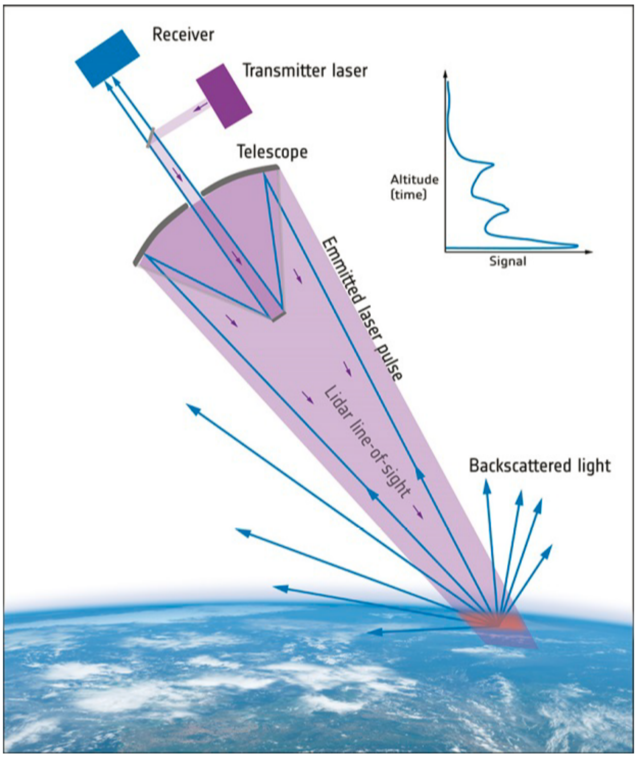

Figure 3.1: Basic scheme of a lidar from space [12].

The transmitter laser produces laser pulses that are emitted into the atmosphere. The light, backscattered from particles and air molecules within the LOS is collected by the telescope and transmitted to the receiver. The analysed signals are used to determine vertical profiles of different properties of the atmosphere [14]. Thanks to the rapid development of laser technique and detecting systems, the lidar has established itself to be a reliable system for remote monitoring of atmospheric properties. The field of application is thereby large. Depending on the technical setup of the lidar, it is possible to distinguish between ice crystals and water droplets in clouds, to provide aerosol classification according to size, shape and absorption properties, to observe trace gases like ozone or water vapour and also to determine wind velocities [16].

The basic lidar equation to describe the detected backscattered signal is thereby [16]:

$$P(R,\lambda) = P_0 \frac{c\tau}{2} A\eta \frac{O(R)}{R^2} \beta(R,\lambda) \exp\left[-2\int_0^R \alpha(r,\lambda)dr\right] \tag{3.1}$$

with

P(R, λ)	=	power received from range R	c	=	speed of light
P_0	=	average transmitted power during the laser pulse	τ	=	laser pulse duration
η	=	receiver efficiency	β(R, λ)	=	atm. backscatter coefficient
A	=	receiver area of the telescope	α(R, λ)	=	atm. extinction coefficient
λ	=	emitted wavelength	O(R)	=	overlap function
R	=	range of scattering volume			

The measurable quantities, that provide information about the atmosphere are the backscatter and the extinction coefficient. The first one describes how much light is scattered from the atmosphere back to the lidar and is mainly responsible for the strength of the lidar signal. In the atmosphere it results from the scattering at air molecules and particles and can therefore be written as [16]:

$$\beta(R,\lambda) = \beta_{\text{mol}}(R,\lambda) + \beta_{\text{par}}(R,\lambda) \tag{3.2}$$

The extinction coefficient characterizes how much light is absorbed or scattered in other directions than 180° on the way through the atmosphere. The whole exponential expression results from the Lambert-Beer-Law and describes the transmission of the atmosphere due to extinction. The factor 2 appears because of the two-way transmission path. Likewise for backscatter, extinction in the atmosphere can result from scattering/absorbing at molecules as well as at particles [16]:

$$\alpha(R,\lambda) = \alpha_{\text{mol}}(R,\lambda) + \alpha_{\text{par}}(R,\lambda) \tag{3.3}$$

The scattering behaviour of the laser light at molecules and particles is described by two different scattering types:
Rayleigh scattering appears on objects which are much smaller than the scattered wavelength. For the emitted wavelength of ALADIN this is valid for air molecules.
The second type is called Mie scattering and occurs on spherical objects which have the same magnitude as the scattered wavelength, like spherical particles in this case.

The molecular backscatter coefficient, β_{mol}, is derived from the Rayleigh theory and is proportional to the atmospheric density. It depends on the number of molecules per m^3 (N_{mol}) and the backscatter cross section per molecule (σ_{mol}) [14, 16]:

$$\beta_{\mathrm{mol}}(z) = N_{\mathrm{mol}}(z) \cdot \sigma_{\mathrm{mol}} \tag{3.4}$$

with

$$N_{\mathrm{mol}}(z) = \left[\frac{273.15\mathrm{K}}{T(z)}\right] \cdot \left[\frac{p(z)}{1.01325 \times 10^5\mathrm{Pa}}\right] \cdot N_L \tag{3.5}$$

and

$$\sigma_{\mathrm{mol}} = \left[\frac{0.55 \times 10^{-6}\mathrm{m}}{\lambda}\right]^4 \cdot 5.45 \times 10^{-32}\mathrm{m}^2\mathrm{sr}^{-2} \tag{3.6}$$

$N_L = 2.68 \times 10^{25}$ m^{-3} is called the Loschmidt's number and is the number of molecules per m^3 for the conditions $T = 273.15$ K and $p = 1.01325 \times 10^5$ Pa. As the formulas 3.5 and 3.6 show, the molecular backscatter coefficient only depends on the vertical temperature and pressure profiles and the emitted wavelength. The wavelength of the lidar is known and the vertical temperature and pressure profiles can be derived by radiosondes, lidars or atmospheric models. Thus, it is possible to calculate β_{mol} independently from the lidar measurements.
Furthermore, the extinction coefficient is proportional to β. The correlation is called *Lidar ratio* (L):

$$L = \frac{\alpha}{\beta} \tag{3.7}$$

and depends on shape, size and absorption behaviour of the scattered molecule/particle [17].

The molecular lidar ratio is well known [16]:

$$L_{\mathrm{mol}} = \frac{\alpha_{\mathrm{mol}}}{\beta_{\mathrm{mol}}} = \frac{8\pi}{3}\ \mathrm{sr} \tag{3.8}$$

It should be mentioned that in this formula α_{mol} refers only to the molecular extinction due to scattering $\alpha_{\mathrm{mol}_{\mathrm{sca}}}$. The molecular extinction due to absorption $\alpha_{\mathrm{mol}_{\mathrm{abs}}}$ is assumed to be zero. That differs when wavelengths are used which are in the absorption range of molecules.

Regarding the lidar equation 3.1, there are still two unknown variables β_{par} and α_{par} within one equation, correlated by an unknown particle lidar ratio L_{par}. There are several methods to solve this problem. One is called the *Klett method* [18], in which the lidar ratio is assumed. Another possibility is to measure two individual lidar profiles, one with and one without the particle backscatter coefficient ($\beta_{\mathrm{par}} = 0$). This is either realised by the *Raman method* [19], that measures additionally the inelastic, thus frequency-shifted Raman backscatter of molecular nitrogen and oxygen, or by the HSR method [20]. The second method uses the different spectral shapes of the backscattered signal from molecules and particles, which can be measured separately. This method is used on ALADIN and will be further explained in the following sections.
In case of the ALADIN instrument its two receiver channels are named by the scattering types that they are able to measure - the Rayleigh channel, focused on molecular scattering and the Mie channel focused on particle scattering.

3.2 Measurement principle of ALADIN

The idea of wind measurements is to consider the superimposed movement of molecules and particles in the atmosphere. For this the principle of the optical Doppler effect is used. It describes the frequency shift of a wave, caused by the relative motion between the source and the observer of the wave [14]. In case of wind measurements, the molecule or particle has a relative velocity along the LOS v_{LOS} to the transmitted laser pulse with a wavelength λ_0. Therefore a frequency shift of the transmitted frequency $f_0 = \frac{c}{\lambda_0}$ occurs on the scattered molecule/particle. As for the backscattered laser pulse the molecule/particle acts as a moving source, a second shift occurs on the backscattered light. Consequently, the detected signal on the lidar receiver has a double frequency shift on top of the transmitted frequency [16]:

$$f = f_0 + \Delta f = f_0 \pm 2\frac{v_{\mathrm{LOS}}}{\lambda_0} \tag{3.9}$$

Δf describes the whole frequency shift which is either positive or negative, depending if the

particle movement is towards or away from the lidar.
As already mentioned, wind is the superimposition of the individual movement of particles and molecules. While particles have a higher mass and move slow, molecules have a high thermal, random movement, called Brownian motion. It strongly depends on the pressure and temperature and is much faster than the wind velocity. Therefore molecules have a naturally broad frequency shifted scattered spectra, while particles have a narrow spectra [14]. However, both spectra are shifted by the same amount due to the wind velocity. Figure 3.2 shows the backscattered spectral density with the frequency shift as x-axis. The solid line describes the spectra at zero wind and the dashed line correspond to a LOS velocity of $v_{\mathrm{LOS}} = 50\ \mathrm{ms}^{-1}$ which results in a 282 MHz Doppler shift (that corresponds to a Doppler shift wavelength of $\Delta\lambda \approx 0.118$ pm) [13]. The spectrum is Gaussian line shaped for the molecular scattering and has a narrow peak on the top caused by the particle scattering.

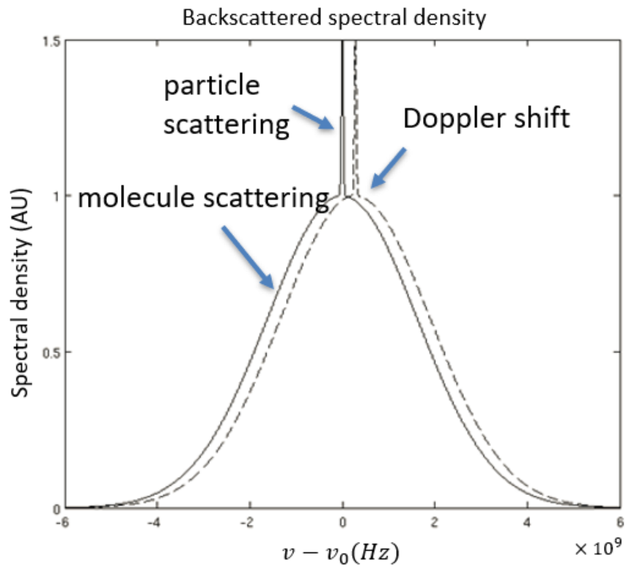

Figure 3.2: Sketch of the backscattered spectral spectrum of molecule scattering and particle scattering at zero wind (solid line) and Doppler shifted at a wind velocity of $v_{\mathrm{LOS}} = 50\ \mathrm{ms}^{-1}$ (dashed line) [13].

3.3 Optical architecture

Mie spectrometer

The Mie spectrometer (MSP) is a Fizeau interferometer consisting of two reflecting plates formed like a wedge. It is used to detect the particle scattering signal. The interferometer acts as a filter by transmitting only the narrow bandwidth in the central part of the returned scattered spectrum, including the particle signal superimposed on the broadband molecule and background signal [14]. The Doppler shift is visualized by a shift of the interference pattern on the detector due to the wedge angle. The useful spectral range (USR) of the Fizeau interferometer, that is imaged on the detector has a range of USR = 0.63 pm or 1500 MHz. The Mie spectrum itself has a Full Width at Half Maximum (FWHM) of FWHM = 0.067 pm or rather 159 MHz [13]. The upper part of Figure 3.3 illustrates the filter function of the Fizeau interferometer. On the left hand side the situation for zero wind is shown and on the right hand side for a non-zero wind. The blue line correspond to the combined Mie and Rayleigh spectra and the red line shall emphasize the small inlet of the Fizeau interferometer. On the lower Figures the signal change on the detector due to the shift is shown. The detection system will be explain later.

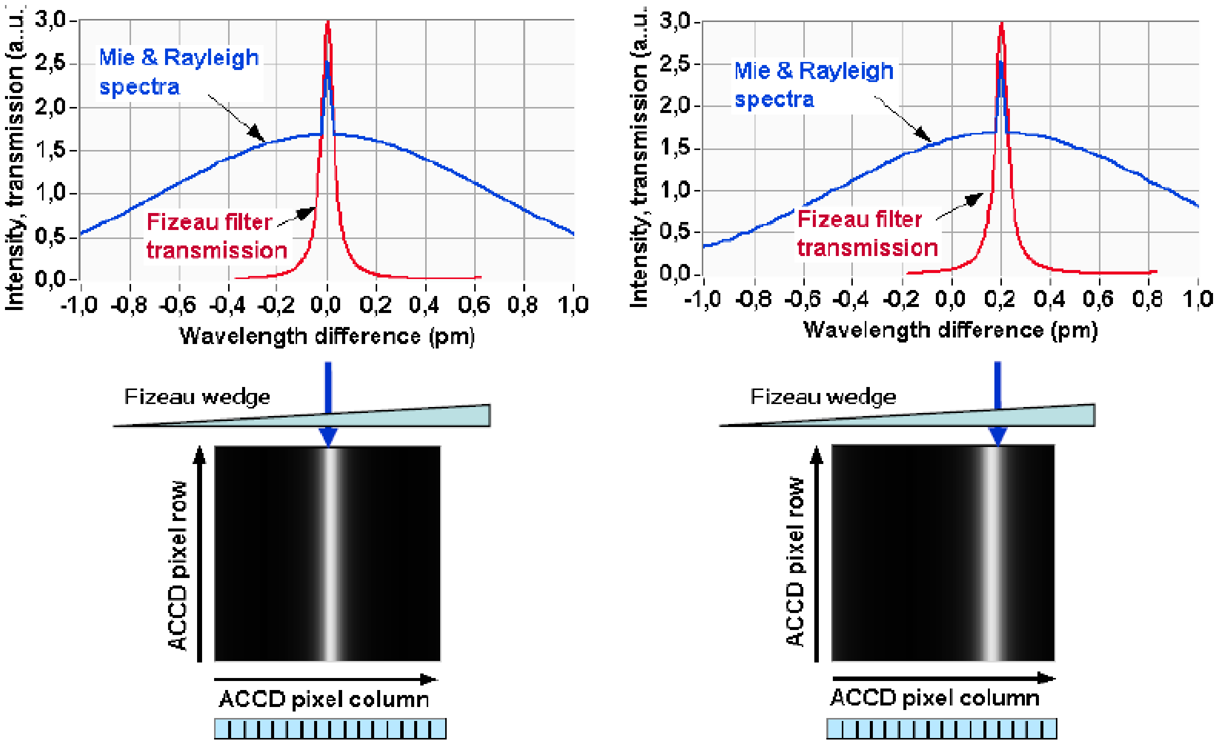

Figure 3.3: Illustration of the function of the Fizeau interferometer. Left: Situation with zero wind. Right: Situation with a non-zero wind [14].

Rayleigh spectrometer

The Rayleigh spectrometer (RSP) consists of two Fabry-Perot interferometers (Filter A and B), using the double-edge technique [21]. The filters are placed at the edge of the transmission curve of the molecular scattering, to be affected by the maximum change of the spectra in case of Doppler shifting. In Figure 3.4 the basic principle of the Rayleigh spectrometer is shown.
On the upper left hand side the situation of zero wind is illustrated. The red line describes the Rayleigh spectrum. On its edges, Filter A and B are placed and record the same transmission. The upper right hand side illustrates the situation with a non-zero wind. Here the spectrum has moved towards filter B. Consequently it has a higher transmission than filter A. The lower

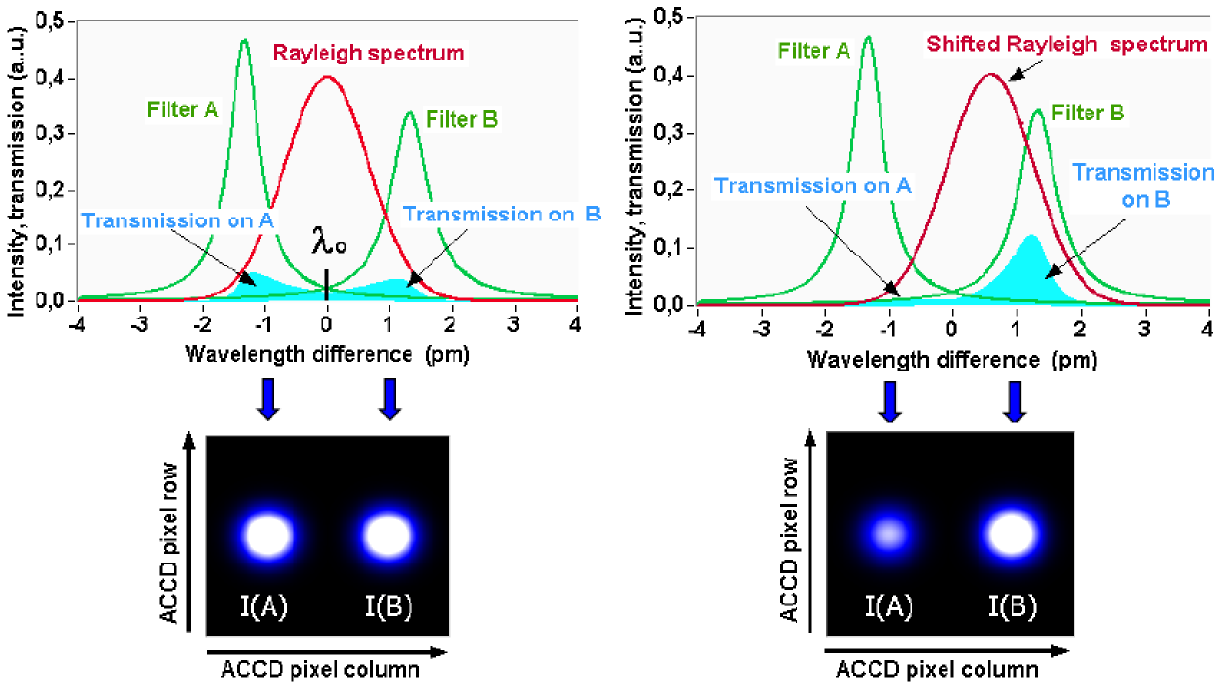

Figure 3.4: Principle of a double-edge Rayleigh spectrometer with no wind (left hand side) and a non-zero wind (right hand side) [14].

Figures show the intensity change of the signals on each filter, due to the shifting.
Calling A and B the number of photons counted after the transmission through the filters, the following relation for the wind velocity can be derived [16]:

$$f(v_{\mathrm{LOS}}) = \frac{\mathrm{A} - \mathrm{B}}{\mathrm{A} + \mathrm{B}} \tag{3.10}$$

$f(v_{\mathrm{LOS}})$ describes a wind depended function. Ideally the Rayleigh wind is independent of the Mie wind. But the Fabry-Perot interferometers have a small overlap within the centre of the spectrum. The measured values A and B are contaminated by the background within this overlap. Furthermore, if a strong Mie peak exists and is shifted towards one filter, the values within the overlap will increase for one filter and decrease in the other but not with the same amount. These effects have to be corrected to reach a representative wind velocity. Additionally, the Rayleigh spectrum has a strong temperature dependency which also needs to be corrected.

Detection system

For the detection of the lidar signal an Accumulation Charge Coupled Device (ACCD) photodetector is used. It consists of an image zone with 16×16 pixels for the spectral resolution and a memory zone with 25 rows which are equivalent to the vertical resolution [14]. This means

the backscattered signal is transmitted through the MSP or RSP and detected on the image zone of the ACCD. From there it is transferred to the memory zone. Then the next signal on the image zone is transferred to the next row of the memory zone and so on. Each row in the memory zone stands for one vertical layer. The duration of the transfer limits the minimum vertical resolution to 250 m.
In case of the Mie channel, the backscattered light of the Mie spectrum is shown on the ACCD. The image zone of the ACCD corresponds to 16 spectral columns and covers the USR of the Fizeau interferometer with the range of 1500 MHz. This leads to a spectral width for each column of 93.75 MHz, which corresponds to a velocity of 17 ms^{-1}. The Mie spectrum (FWHM = 159 MHz) itself covers 1.7 pixels [13]. The different pattern on the image zone due to the Doppler shift is shown in the lower part of Figure 3.3.
In case of the Rayleigh channel, the ACCD is separated into two halves, 8 columns for filter A and B each. As shown in the lower part of Figure 3.4, the intensity on each filter and therefore on the ACCD is equal in the case of zero wind. Whereas for a non-zero wind and thus a Doppler shift, the intensities on the filters differ. The ratio of the different intensities determines the measured velocity [13].

ALADIN structure

The principal optical architecture of the ALADIN instrument is shown in Figure 3.5. On the left hand side it has two Power Laser Heads (PLH), one nominal and one redundant, each connected to a Reference Laser Head (RLH n, and RLH r). A Flip-Flop Mechanism (FFM) switches between both lasers. In the upper right hand side the telescope is shown. It is the same telescope that transmits the laser beam to the atmosphere and receives the backscattered signal.
Everything shown in the Figure within the dashed red line belongs to the Optical Bench Assembly (OBA) and includes the Transmit-Receive Optics (TRO), the MSP with the Detection Front-End Unit Mie (DFU-M) and the RSP with the Detection Front-End Unit Rayleigh (DFU-R). Within the OBA several optical instruments are used:

HWP:	half-wave plate
Pol:	polarising beam splitter
QWP:	quarter-wave plate
LCM:	laser chopper mechanism
IFF:	interference filter

The laser pulses are guided from the PLH through the TRO (red beam). On the Pol they are reflected towards the telescope. After the beam is expanded, it is transmitted to the atmosphere with a circular polarization. The backscattered signal is received by the telescope and transmitted to the OBA. This time the Pol is transmitting the signal towards the optical

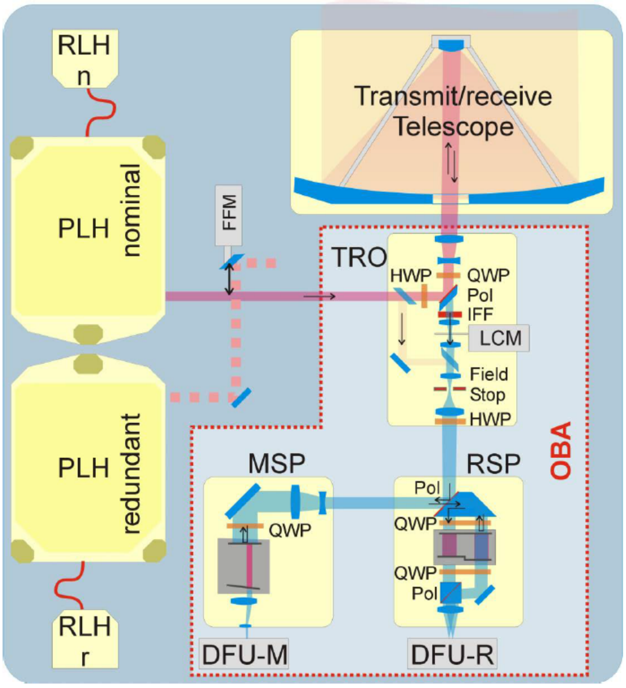

Figure 3.5: The scheme of the ALADIN instrument [14].

receivers, but only the parallel component of the backscattered light. There it is first reflected via another Pol to the MSP, to filter the Mie signal and then backscattered to the RSP, to analyse the Rayleigh signal. In the DFU-M and DFU-R the separated signals are detected by the ACCDs [14].

3.4 Simulation example

For a better understanding of the wind measurements, a simulation example of the Aeolus wind profiles is shown in Figure 3.6.

The simulation starts at the equator and performs one orbit around the earth. Figure 3.6 (a) and 3.6 (b) are the simulation input from an ECMWF model of the "truth" HLOS wind and the typical cloud properties. The HLOS wind input shows the typical global wind structures, like the Subtropical and Polar jet streams and the Polar vortex. The sign of the wind depends if the wind is directed towards or away from the LOS and changes with the viewing direction of Aeolus.

Figure 3.6 (c) and 3.6 (d) show the simulated output from the Rayleigh channel and the Mie channel. The vertical resolution is divided into 24 layers and differs between 250 m (at the PBL) and 2 km (in the lower stratosphere). The Rayleigh channel measures the wind in the clear-sky scenario. Without any clouds its measuring range is from 0 km to almost 30 km. But the simulation shows, that it cannot measure in a cloudy scenario. For this, the Mie channel is

(a) Simulator input "truth" HLOS wind (ms^{-1})

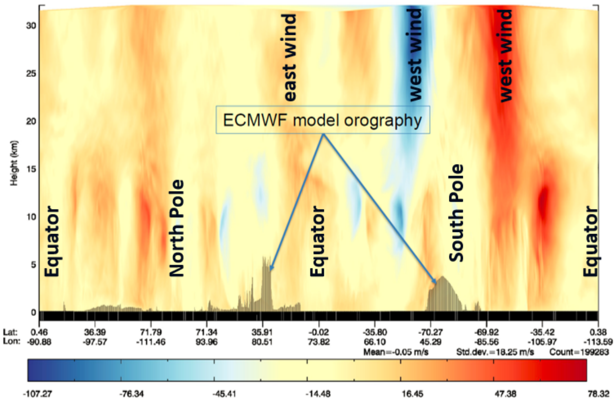

(b) Simulator input scattering ratio

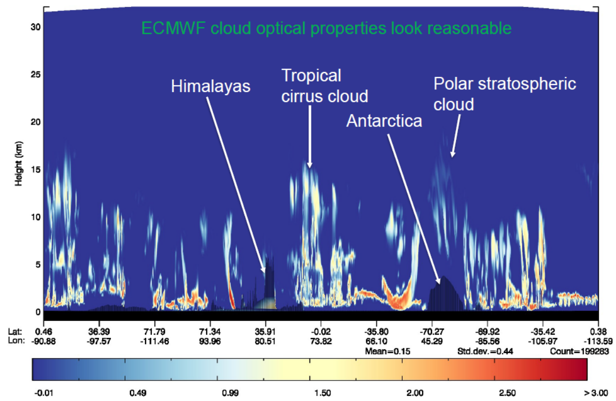

(c) Rayleigh$_{clear}$ HLOS wind (ms^{-1})

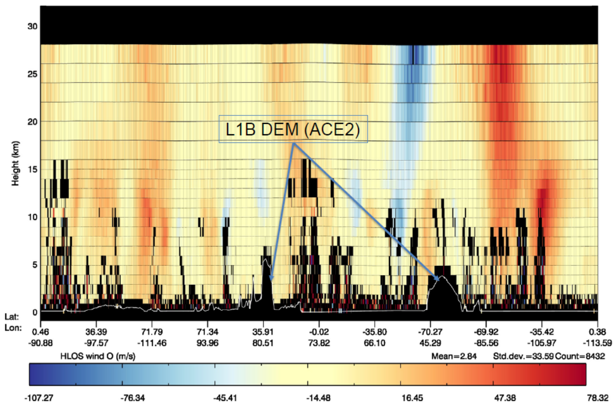

(d) Mie$_{cloudy}$ HLOS wind (ms^{-1})

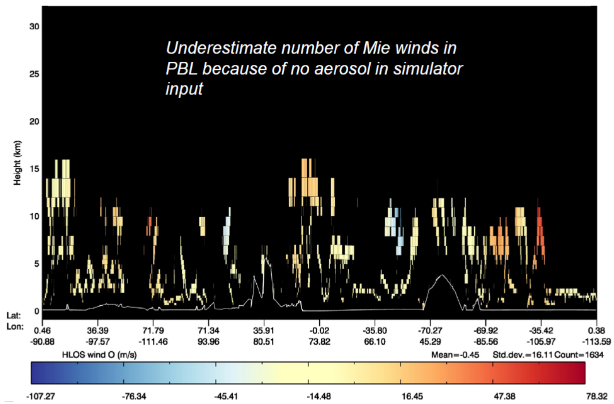

Figure 3.6: Simulation input of the "truth" HLOS wind (a) and the typical cloud properties (b) from the ECMWF model. Simulation output of the Rayleigh$_{clear}$ HLOS wind (c) and the Mie$_{cloudy}$ wind (d) [15].

suitable which measures the wind in cloudy/aerosol conditions. However, its range is limited by the top of thick clouds as it can not penetrate through them. It should be mentioned that the simulation does not include the aerosol layers. The combination of the Rayleigh$_{clear}$ and the Mie$_{cloudy}$ wind profiles result in an exhaustive profile, with a maximum possible wind measurement cover.

3.5 Aerosol and cloud property measurements

Besides wind profiles, Aeolus can provide aerosol and cloud properties. As ALADIN is a HSR lidar, having the Rayleigh and Mie channel, it measures the particle extinction and particle backscatter coefficients independently. From these two properties it is possible to determine the lidar ratio L (see formula 3.7), which depends on shape, size, and absorption properties of the aerosols and cloud particles [17]. However, ALADIN has a large disadvantage for the aerosol and cloud classification. As it has the same telescope for the outgoing and the

receiving signal (see Figure 3.5), only the co-polarized component of the backscattered light can be detected. At highly depolarizing aerosols, like ice particles, desert dust or ash, the cross-polarized component can be much higher than the co-polarized. This results in an underestimation of the particle backscatter coefficient and therefore an overestimation of the lidar ratio up to 50% to 75% for ice clouds and up to 50% for the appropriate aerosols [13].
For this reason it is necessary also to perform validations for aerosol products to determine the quality of aerosol and cloud classification by the ALADIN instrument and to develop respective corrections.

4 Challenges of the Aeolus mission [1]

Being an explorer mission does not only mean new technical achievements, but also many unforeseen challenges during the mission. For this, analysis of the Aeolus product qualities are made to identify problems and improve the Aeolus measurement products. The analysis are performed in the frame of the Aeolus Scientific Calibration & Validation Team (ACVT), the Aeolus Data Innovation and Science Cluster (Aeolus DISC), and the Aeolus Science and Product quality Working Group (SAG). Furthermore, in total 26 calibration and validation (CAL/VAL) teams of different nations, including the German initiative EVAA, are validating the Aeolus products, comparing them to different NWP models, radiosondes, balloon, ground-based, aircraft, and satellite measurements. The ensuing problems need to be discussed and examined to learn from them and to improve the technology in further similar missions. This chapter describes the state of the Aeolus mission, providing informations about the main challenges, like the decrease in laser energy, the lower receive transmission and the increase of the dark signal of individual pixels.

Hot pixel

During the commissioning phase of Aeolus it was noticed, that in the memory zone of both ACCD cameras, pixels with an increased dark current signals occurred. Depending on the position of the pixel, the increased dark current can lead to a bias of individual wind and aerosol range-bins. These pixels are called *hot pixel* and have a fluctuated strength over time. Also the number of hot pixels is growing as every few weeks a new pixel occurs. The reason why they appear is not yet clearly known. Several assumptions were made but could not be proved yet. Figure 4.1 and table 4.2 shows the actual number and position on the ACCD of the hot pixels for the Rayleigh and Mie channel as valid until the 23 October 2019.
For the characterization and calibration of the hot pixels, a new instrument mode was developed. The correction was implemented into the operational processor on 14 June 2019. Besides for the last comparison profile, shown in this thesis, the new correction is not yet

[1] The presented challenges of the Aeolus mission and the following validation includes preliminary data (not fully calibrated/validated and not yet publically released) of the Aeolus mission that is part of the European Space Agency (ESA) Earth Explorer Program. Further data quality improvements, including in particular a significant product bias reduction, will be achieved before the public data release. The analysis has been performed in the frame of the Aeolus Scientific Calibration & Validation Team (ACVT), the Aeolus Data Innovation and Science Cluster (Aeolus DISC) and/or the Aeolus Science and Product quality Working Group (SAG).

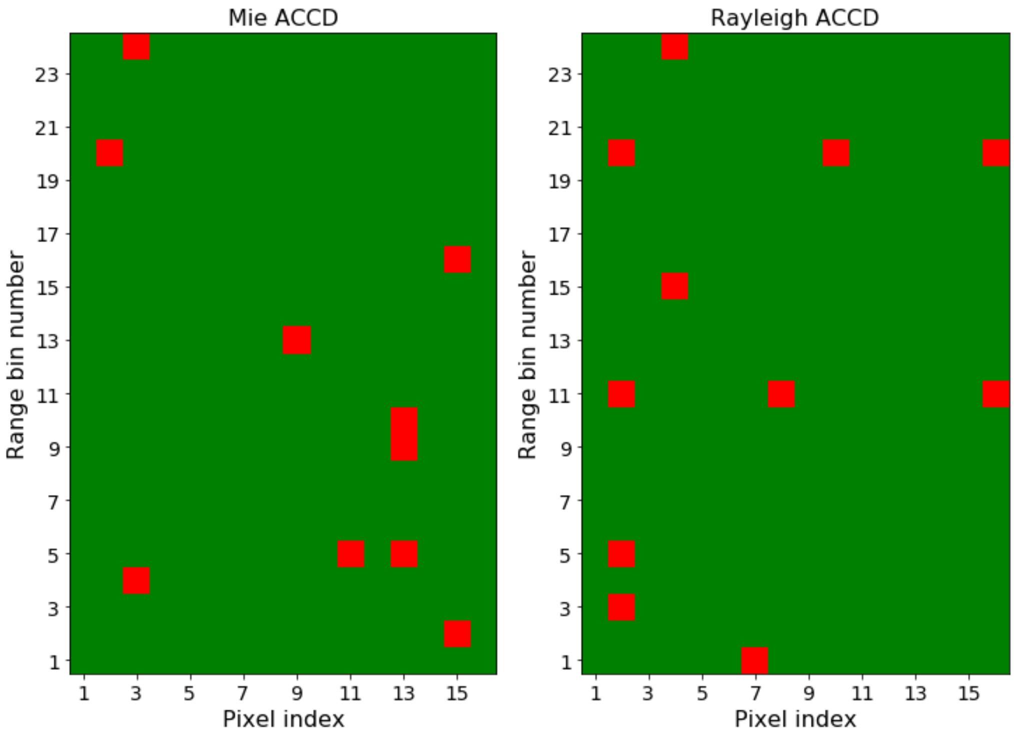

Figure 4.1: Red pixels: Illustrate the position and number of hot pixels on the Rayleigh and Mie ACCD (The Plot is taken from the internal Aeolus wiki page, accessible for CAL/VAL teams, visited on 23.10.2019).

(a) Mie channel

Range bin	Pixel index	Starttime
16	15	before IOCV
24	3	before IOCV
13	9	2018-10-21
2	15	2018-10-24
5	13	2019-01-09
20	2	2019-03-31
10	13	2019-04-26
9	13	2019-08-08
5	11	2019-10-03
4	3	2019-10-03

(b) Rayleigh channel

Range bin	Pixel index	Starttime
11	2	2018-09-07
5	2	2018-11-04
15	4	2018-11-24
20	10	2019-01-27
1	7	2019-02-20
11	16	2019-03-17
3	2	2019-05-08
11	8	2019-06-15
20	2	2019-08-01
20	16	2019-08-17
24	4	2019-08-29

Figure 4.2: Listed hot pixels with range bin position, pixel index, and start time (The data is taken from the internal Aeolus wiki page, accessible for CAL/VAL teams, visited on 23.10.2019).

available for the time of the validation of this thesis, which is why the altitudes of the bins including hot pixels are excluded in the rest of the comparisons.

Wind measurement biases

Comparisons of Aeolus measurements with NWP models show time-varying biases in the wind velocity. On the Aeolus CAL/VAL workshop in March 2019 [22] several characteristics and probable causes were discussed: First of all, a global, slowly linear drifting constant bias is observed. It is caused by a drift in the instrument response, due to laser instrument changes. Enhancement should be possible by a time-varying calibration strategy. Additionally, a harmonic bias with orbit phase appears. The reasons are not totally clear, but evidence indicates that it might be related to changes of the ALADIN telescope temperature associated with solar background levels and imperfect correction of the LOS pointing knowledge. By the improvement of the correction and a zero wind calibration using ground returns, a mitigation should be possible. Last but not least, the hot pixel problem discussed before result in a bias for single range-bins, but a correction algorithm is meanwhile available.

Laser energy development

Another challenge was discovered shortly after the switch on of the first ALADIN laser. From pre-launch tests, the emitting ultra violet (UV) laser energy was expected to be at 80 mJ. But after the switch on, the UV output energy started at a lower value of around 65 mJ. Figure 4.3(a) shows the UV and infrared (IR) energy development for the first laser from the beginning until 16 June 2019. Since the start it strongly decreased to only 40 mJ in mid June 2019. This decrease is assumed to be related to temperature sensitivities within the instrument. With thermal optimizations and sensitivity tests it was tried to counteract, which results in short-term increases of the energy, but it did not stop the constant downward development. The lower laser energy influences the random errors of the measurements. Analyses[1] presented on the Aeolus CAL/VAL workshop [22] report that even with the highest energy of 65 mJ, the error is increased by a factor of around 1.14 to 1.26 compared to the one with the original expected energy of 80 mJ. With further energy decrease, the random error increases more, which is why it was decided to switch to the second laser on 16 June 2019. It is hoped that it has a more stable energy than the first one. Figure 4.3 (b) shows the output energy development of the second laser until 16 October 2019. It is now higher than 60 mJ and does not yet show the strong decrease as the first laser. Still, the observation of the development needs to be continued.

[1] not publically accessible

(a) Output energy of laser A

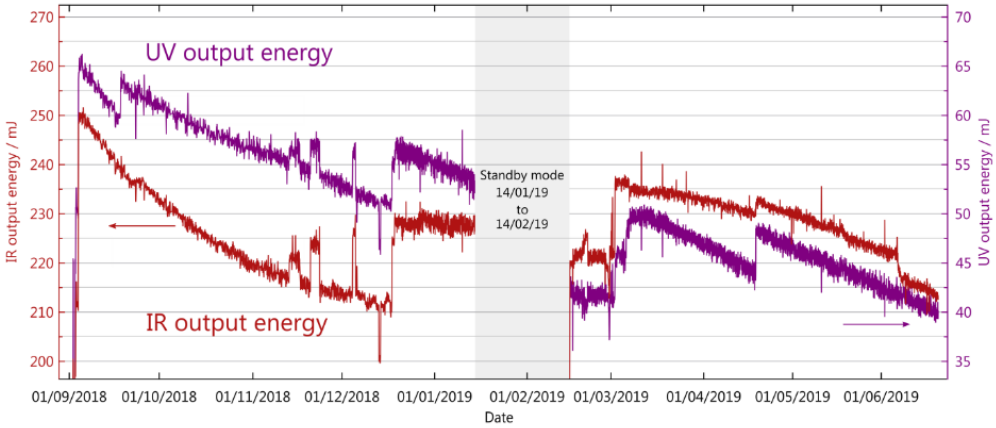

(b) Output energy of laser B

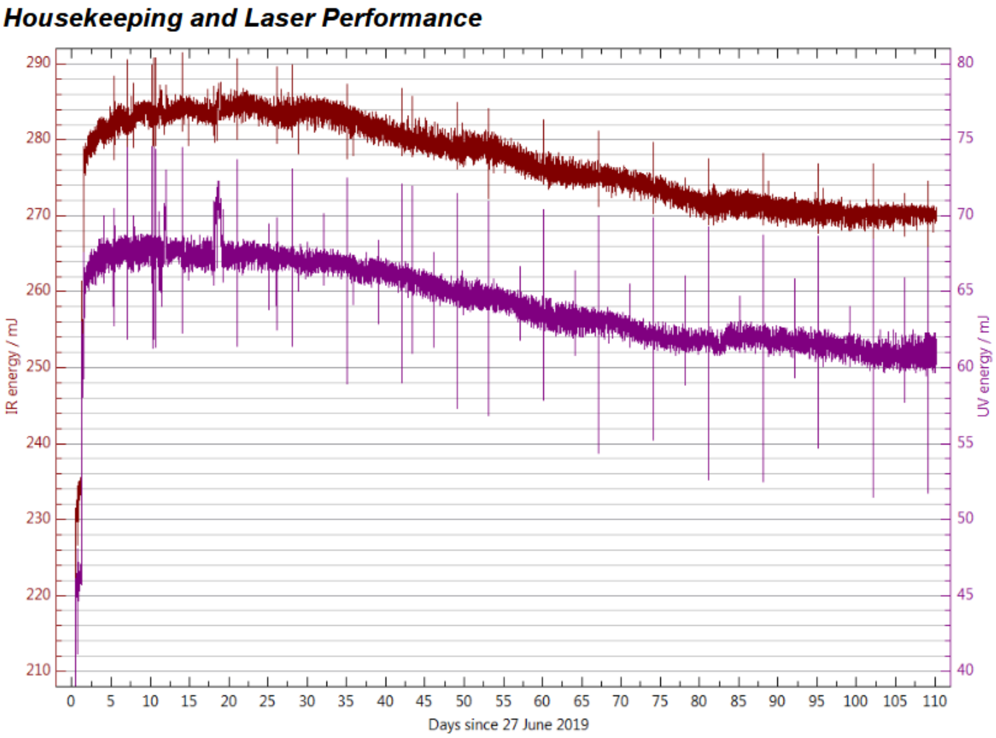

Figure 4.3: The UV and IR output energy development of the first ALADIN laser (a) and the second laser (b) (The Plots are from the internal weekly data quality reports, accessible for CAL/VAL teams, visited on 23.10.2019).

Receive transmission

Another unforeseen problem is a lower atmospheric return signal than expected. On the Aeolus CAL/VAL workshop [22], comparisons of in-orbit measurements and pre-launch simulation were shown, in that the Rayleigh returned signals are by a factor of 2.5 to 3.0 lower, assuming 80 mJ in the simulation or rather 1.6 to 2.0 lower, using the actual laser energy. Also the ground return signals for high-albedo ice is lower than expected for the Rayleigh as well as the Mie channel. Like the lower emitted energy, the reduced signal leads to an increase of the random wind errors. In the summary report[1] of the first three months and during the Aeolus CAL/VAL workshop [22] several possible reasons were discussed: First of all, the lower emitted energy lowers also the returned signal. Furthermore, ALADINs laser beam appears to have a higher divergence. This leads, together with the non-perpendicular incidence angles, to a clipping of the backscatter signal at the optical receiver field stop. As the field of view is limited by the field stop, it lowers the signal that is passing on to the Mie and Rayleigh spectrometers. Still, further investigations need to be made.

Considering all the different factors that are increasing the random errors of the wind and aerosol measurements, the random error is estimated in the summary[1] of the Aeolus CAL/VAL workshop [22] to be $\approx 4\ \mathrm{ms}^{-1}$ for the $\mathrm{Rayleigh}_{\mathrm{clear}}$ and $\approx 2.5\ \mathrm{ms}^{-1}$ for the $\mathrm{Mie}_{\mathrm{cloudy}}$ measurements. The values vary with time, especially increasing with the lower emitted energy before the laser was switched.

[1]not publically accessible

5 Measurement products and data filtering

In this chapter, the most important measurement products and the Aeolus data filtering used for the validation will be explained.

The measurements of Aeolus pass several instrument data processing levels and result in the following products [12, 13]:

AISP, Level 0, Level 1A:
In these products the data preparation is progressed. The raw data Annotated Instrument Source Packet (AISP) is time ordered (Level 0) and the geolocation of the data as well as the calibrated house-keeping information is included (Level 1A). This data is not accessible for CAL/VAL teams and other users.

Level 1B:
Preliminary HLOS wind with basic corrections and calibrations. The temperature and pressure correction that are necessary for the wind measurements at air molecules are not yet included. Level 1B is the first product available for the users.

Level 2B:
Fully calibrated and processed HLOS wind, ready for data assimilation in NWP models.

Level 2C:
Vector wind data, resulted from ECMWF model analysis after the assimilation of Level 2B profiles.

Level 2A:
Additional aerosol/cloud profiles.

For the validation of the Aeolus wind products, the Level 2B product is chosen for comparison to the radiosonde measurements. The output of the product includes different classifications and quality parameters which need to be chosen correctly. Beside the exclusion of the hot pixel range-bins, the following filtering is considered:

Validity flag

This flag considers the validity of the measurement output. It has either the value 1 (valid measurement) or 0 (not valid) [23]. E.g. in case of negative range-bins, the validity flag would be 0. Thus the first filter is to use only measurements with a validity flag of 1.

Atmospheric classification

The atmospheric classification distinguishes between four different types. The Level 2B product provides for each type a separate profile [24]:

Rayleigh$_{\text{clear}}$

Includes the Rayleigh wind derived from measurements with no particle backscatter, thus a clear sky.

Rayleigh$_{\text{cloudy}}$

The Rayleigh wind derived from measurements with non-zero particle backscatter, thus a cloudy environment.

Mie$_{\text{clear}}$

The Mie wind derived from molecular backscatter. As in clear sky condition no Mie wind should be able to detect, this is only possible if the classification failed to detect particle backscatter.

Mie$_{\text{cloudy}}$

The Mie wind derived from particle backscatter.

To select the different scenarios, each range-bin of the measurements in the observation is considered individual. First of all, each range-bin within the 90 km of the observation is sorted to the corresponding atmospheric scenario. The classification can be done by using the scattering ratio, the particle feature finding or the particle extinction coefficient as criteria [24]. The current recommended method is using the scattering ratio. For this, predefined scattering ratio threshold values as a function of altitude are used. If the scattering ratio is higher than the threshold value, the signal is detected as particle scattering. Staying below the threshold, molecular scattering is detected. The range-bins in each classification are counted and assigned with the same weight within the corresponding observation. The accumulation of the measurements improves the signal-noise ratio and provides a large-scale wind observation, which is more useful for the NWP data assimilation [24].
For an accurate Mie wind measurement, a strong particle backscatter is required, whereas the best quality of the Rayleigh measurements is achieved in clear sky conditions. This is why in this validation the wind results of the Rayleigh$_{\text{clear}}$ and the Mie$_{\text{cloudy}}$ types are used, having the least error and most valid measurements.

Error threshold

The Level 2B product provides a HLOS error estimation for each range-bin in the profiles. The recommended limits from the ESA Aeolus team are < 8 ms^{-1} for the Rayleigh$_{\text{clear}}$ and < 3 ms^{-1} for the Mie$_{\text{cloudy}}$ error. As in this validation the number of comparisons and therefore the available Mie$_{\text{cloudy}}$ measurements is small, the limit for the Mie$_{\text{cloudy}}$ error is raised to < 5 ms^{-1} to include more measurements.

6 Aeolus Validation

In this chapter the radiosonde and lidar profiles will be compared to the Aeolus wind and aerosol profiles and its quality discussed. The first part focuses on the wind and aerosol measurements during the Polarstern cruise and second one on the wind measurements performed in Leipzig.

6.1 Shipborne validation

The shipborne validation took place during the Polarstern cruise PS116 (10 November 2018 to 11 December 2018) from Bremerhaven to Cape Town [7]. Figure 6.1 shows the track of the cruise and the positions of each day at 12 UTC (blue dots).

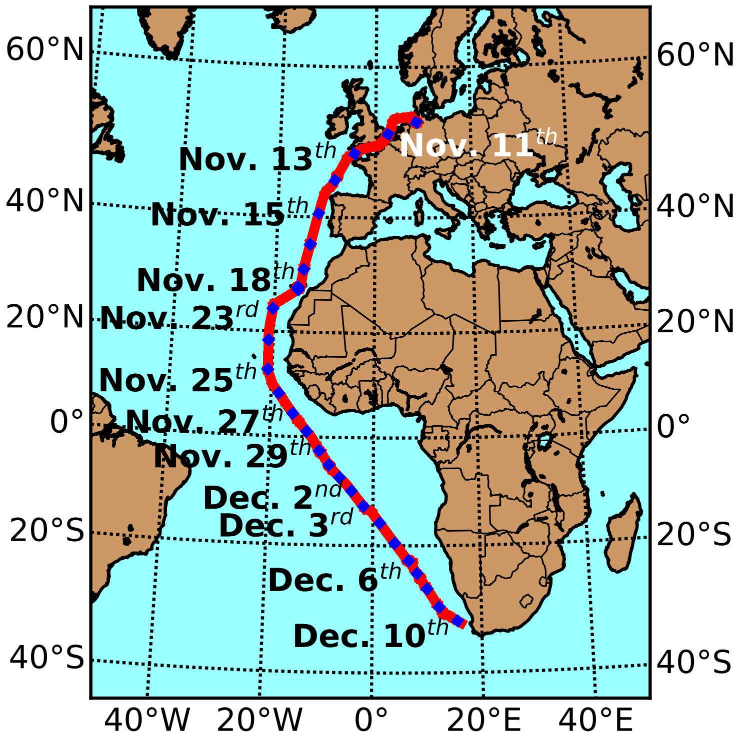

Figure 6.1: Cruise track PS116 of Polarstern from Bremerhaven to Cape Town between 11 November 2018 and 10 December 2018. The blue dots are the positions of each day at 12 UTC (Plot created by Kevin Ohneiser).

On board was the portable multiwavelength Raman polarization lidar Polly^{XT} of the OCEANET facility [10]. With its setup, aerosol and cloud properties can be classified by shape, size, and absorption behaviour [17, 25]. Figure 6.2 gives an overview of the atmospheric conditions during the Polarstern cruise. The upper Plot shows the uncalibrated attenuated particle backscatter coefficient at 1064 nm and the lower Plot the corresponding volume depolarization ratio. The measurement gap between 18 November 2018 and 22 November 2018 is caused by the stay in Gran Canaria, where Polarstern had no permission to perform measurements. The blue colour in the Plots indicates no particle backscatter signal or rather no volume depolarization, thus spherical or no particles. The green colour in the upper Plot indicates an aerosol layer, as the lidar receives particle backscatter, but not as much as for cloud layers, which are recognisable by the strong, white coloured signal. For the depolarization ratio, the green colour in the Plot indicates stronger depolarization, that occurs for non-spherical particles or multiple scattering, as in optical thick clouds. The white coloured signals stand for very high depolarization, which is a typical sign of ice clouds [25, 26].

In the Northern hemispheric atmosphere the cruise was characterized by the occurrence of a mixture of high ice and lower water and mixed-phased clouds. After crossing the equator on 28 November 2018, the weather in the first few days was characterized by a constant cover of low clouds, starting at an altitude of 500 m, caused by the trade inversion [8].

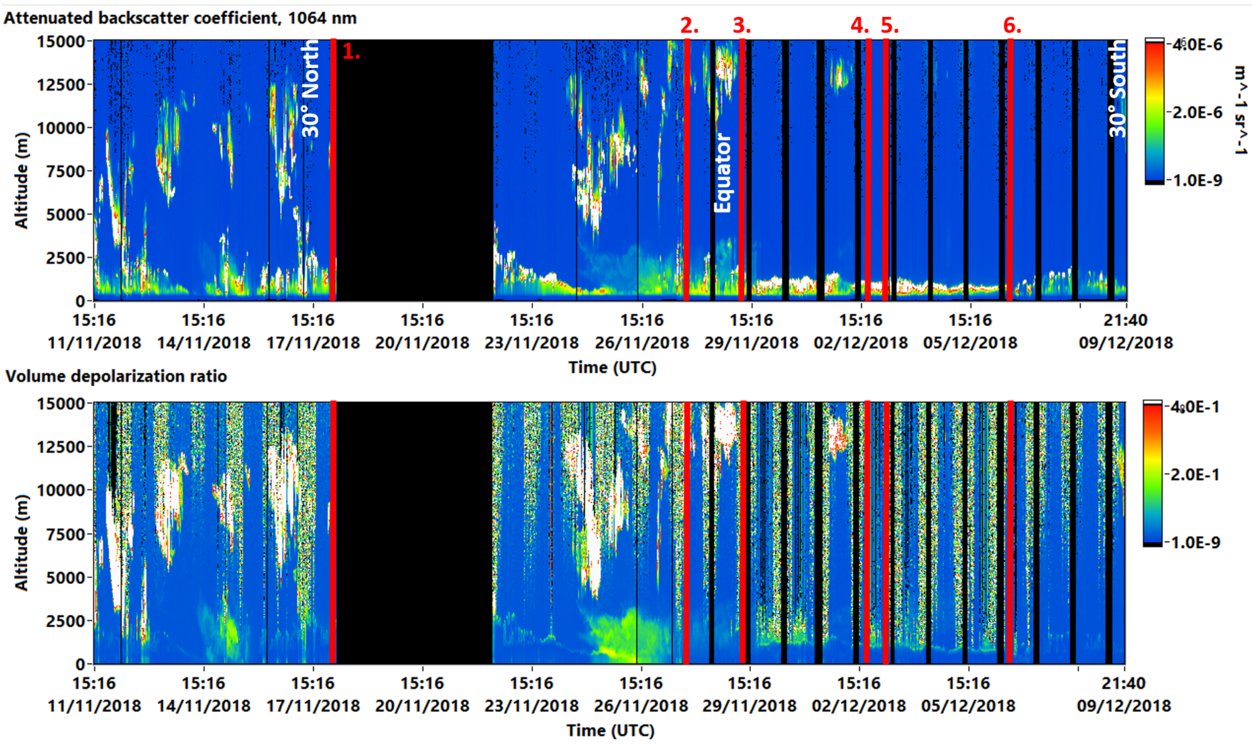

Figure 6.2: The upper Plot shows the uncalibrated attenuated particle backscatter coefficient at 1064 nm and the lower Plot the volume depolarization ratio from Bremerhaven to South Africa for the period of 11 November 2018 to 9 December 2018. The red lines show the points of intersection with the Aeolus overpasses.

The cloud cover opened up while Polarstern was getting more southwards. Interesting though is the dust case, which occurred between 25 November 2018 and 27 November 2018. As dust consists of non-spherical aerosols, it is among other characteristics identifiable in the lower Plot of Figure 6.2 by stronger depolarization ratios in the lower three kilometres. As Aeolus overpassed the Atlantic in the West African area at that time, this case will be discussed more detailed in the aerosol validation in subsection 6.1.2.
For the wind validation, additional radiosondes of the type RS41, produced by the company Vaisala [27] and provided by the DWD [11], with a vertical range up to 30 km were launched at every point of intersection with the Aeolus overpasses.
Figure 6.3 shows the ground tracks of Aeolus along the track of the ship. Each colour marks a different weekday. Along the cruise seven points of intersection with the overpasses of Aeolus within a 150 km radius around Polarstern were possible (yellow circles).

(a) First part of the PS116 cruise

(b) Second Part of the PS116 cruise

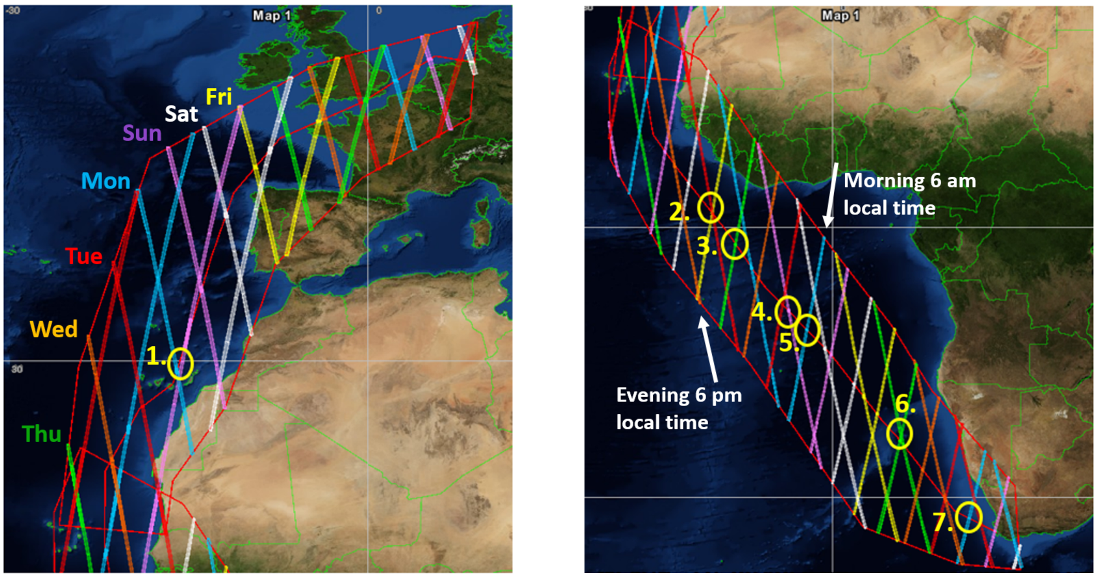

Figure 6.3: Coloured tracks: Ground tracks of Aeolus, each colour represents another weekday. Yellow circles: Points of intersection within 150 km of Polarstern and the Aeolus overpass.

The radius was chosen as a compromise between the number of possible points of intersection and a reasonable limit for significant validation. For Polarstern, it was only possible to reach the position of three overpasses almost directly in time. As the horizontal resolution of the wind products of Aeolus at this time was 90 km and the dominant trade wind circulations are mostly stable above the Ocean, the radius is still in an acceptable range. This radius range is also the recommended limit for all CAL/VAL stations. Still, it is to be expected, that the deviation of the wind measurements of Aeolus and the radiosondes will increase with further distance.

The radiosondes were launched one hour before the overpass. It should be mentioned, that no radiosonde could be launched at the first point of intersection, as Polarstern was already too close to Gran Canaria and had no permission to launch radiosondes. For the same reason no lidar measurement could be done at the last point of intersection, as Polarstern was already in the waters of South Africa.

6.1.1 Wind validation

Case studies

For the first case study, the point of intersection on 29 November 2018 (number 3 in Figure 6.3(b)) is chosen. It could be reached within a distance of $\approx$ 30 km. At that moment, Polarstern had just recently passed the equator. Figure 6.4 shows the range corrected lidar signal at 1064 nm for the time of the overpass. An optical thick cloud layer at around 2 km is indicated here by the white colour, which the lidar signal cannot penetrate. Looking at the signals with no cloud layer, an aerosol layer up to around 4 km is visible, recognisable by the stronger less noisier signal. It will be further discussed in subsection 6.1.2.
Figure 6.5 shows wind velocity profiles measured by the radiosonde (red) and the two closest Aeolus Rayleigh$_{\text{clear}}$ (green and blue) and the Mie$_{\text{cloudy}}$ profiles (magenta and cyan). Plot 6.5 (a) shows the radiosonde profile with its highest vertical resolution. In Plot 6.5 (b) the vertical resolution of the radiosonde measurements is adjusted to the same of the Aeolus range-bins. As Aeolus measures only the wind along the LOS, which is mainly the west-east wind component, the radiosonde measurements are projected to the LOS ($v_{RS_{LOS}}$) side, using the following formula:

$$v_{RS_{LOS}} = v_{RS} \cdot \cos(\varphi_{Aeolus} - \varphi_{RS}) \tag{6.1}$$

v_{RS} describes the original wind velocity of the radiosonde and φ_{RS} its measured wind direction. φ_{Aeolus} is the azimuth angle of Aeolus, which is obtained from the Level 2B data and differs depending on range-bin and global position.

The uncertainty estimation of the radiosonde wind velocity profile is referred to the calculations of the Global Climate Obsvering System (GCOS) Reference Upper-Air Network (GRUAN), which estimates an uncertainty between 0.4 ms^{-1} to 1 ms^{-1} for the wind velocity and 1° for the wind direction [28]. Even though the paper is considering the Vaisala radiosonde type RS92 [29] and not RS41 [27], which was used on Polarstern, there is no significant difference in the uncertainty, as both radiosonde types are based on the same technique to derive wind velocity and direction [30].

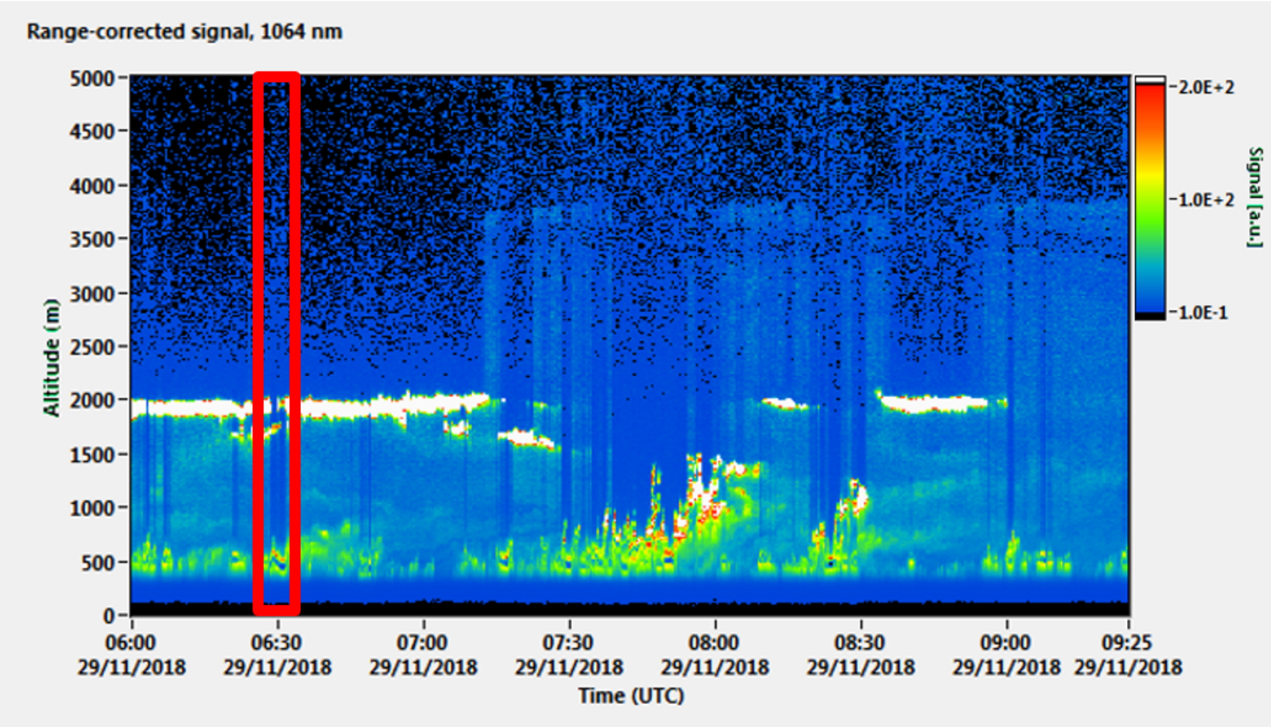

Figure 6.4: The range corrected lidar signal at 1064 nm around the time of the Aeolus overpass (red rectangle) on 29 November 2018.

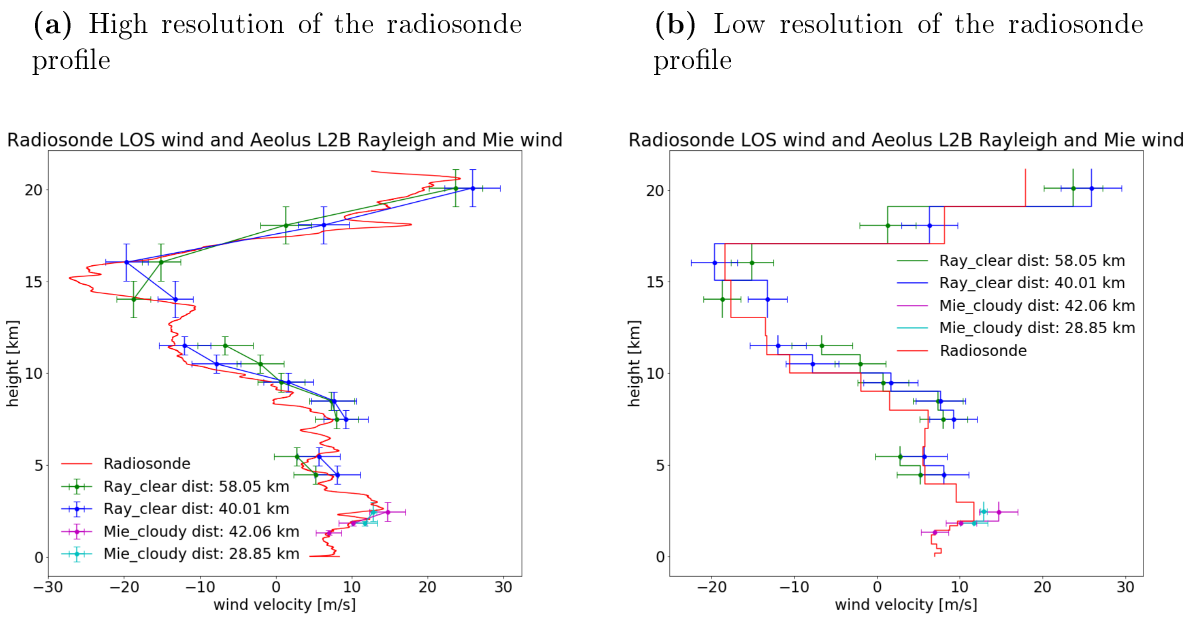

Figure 6.5: Wind velocity profiles measured by the radiosonde (red) with the two closest Aeolus Level 2B (L2B) Rayleigh$_{\text{clear}}$ (green and blue) and Mie$_{\text{cloudy}}$ profiles (magenta and cyan) on 29 November 2018. The radiosonde profile is shown in its highest resolution (a) and with an adjusted resolution to the Aeolus range-bins (b). The radiosonde measurements are projected on the LOS of Aeolus.

Regarding the Mie$_{cloudy}$ profiles in Figure 6.5, only measurements at the altitudes of the cloud layer between 1.2 km to 3 km are provided. Below the cloud cover, ALADIN couldn't receive any signal, as the cloud layer is optically too thick. In Figure 6.5 (a) the Mie$_{cloudy}$ measurements are in good agreement with the radiosonde measurements. In the Plot with the low resolution of the radiosonde wind profile though, a deviation of the Mie$_{cloudy}$ measurement at the altitude of 2.5 km is observed. As for the low resolution the radiosonde wind velocity is averaged along the complete vertical range of the Aeolus bin, the short and rapid decrease of the wind velocity, which is seen in the profile shown in high resolution, is also included. This results in a lower wind velocity in this altitude for the radiosonde profile in low resolution. Regarding the Rayleigh$_{clear}$ measurements, a positive bias in the region between 7.5 km to 12 km is observed. Correcting this bias, it would fit the shape of the radiosonde profile. As discussed in chapter 4, a varying bias of the Aeolus measurements is constantly observed. At the Aeolus CAL/VAL workshop [22], independent comparisons[1] of several CAL/VAL teams showed global biases in the range of < 1 ms^{-1} up to 3.3 ms^{-1}, using different observation periods and NWP models.

While the wind profiles show the, for the inner tropics typical, east trade winds in the lower and mid troposphere, the wind changes to the westerly anti trade wind in the high troposphere, having its maximum wind velocity just below the tropopause at around 15 km [8]. The high resolved radiosonde profile shows a maximum wind velocity higher than 25 ms^{-1}, whereas the high wind velocity of the anti trade wind is not recognized by the Rayleigh$_{clear}$ wind measurements of Aeolus. This is caused by the low resolution of the Aeolus measurements in the higher troposphere/low stratosphere. At that time the Aeolus range-bins had a resolution of 250 m up to 2 km height to perform ground echo characterizations. Above, the resolution is raised to 1 km up to the altitude of 13 km and then to 2 km for higher altitudes. To confirm the problem of the low resolution in the altitude of 15 km, the radiosonde wind measurements are plotted in the same resolution as the Aeolus profiles in Figure 6.5 (b). Here it gets obvious, that the resolution is too low to recognize the strong wind velocity, as the radiosonde profile shows a wind velocity almost 8 ms^{-1} lower than using the high resolved profile. This problem was due to the Commission Phase settings, in which many range-bins near the surface were needed. On 26 February 2019, the range-bins were changed to a resolution of 1 km up to an altitude of 19 km.

The given distance in the legend of Figure 6.5 is the mean distance regarding all vertical bins. As the radiosonde drifts along the wind direction, the distance to Aeolus changes during the measurements. Figure 6.6 (a) shows the trajectory of the radiosonde during the ascent. Regarding the trajectory, the clear change between predominant easterly wind in the low and mid troposphere to the predominant westerly wind in the upper troposphere is seen. When reaching the tropopause, it changes to easterly wind again. In Figure 6.6 (b), the distance

[1] not publically accessible

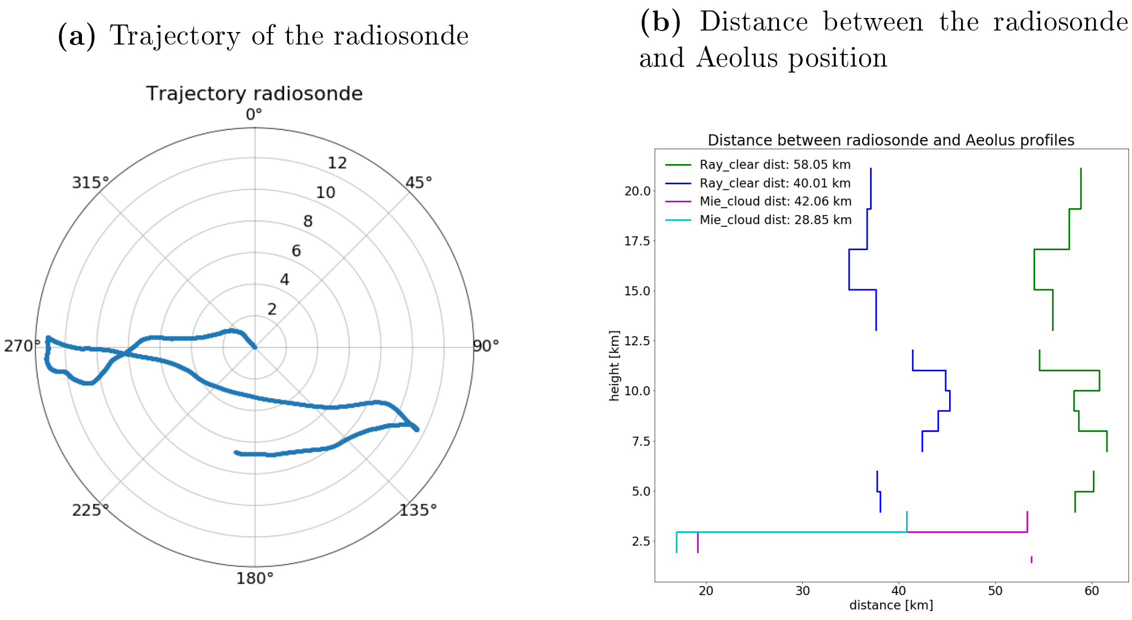

Figure 6.6: Trajectory of the radiosonde on 29 November 2018 (a). The radius is the distance, given in km. The distance between the radiosonde and the Aeolus position along the vertical range (b).

between radiosonde and the Aeolus position is shown. While the distance to the $\text{Mie}_{\text{cloudy}}$ profiles varies quite large in the lower 5 km, the distance to the $\text{Rayleigh}_{\text{clear}}$ profile above 5 km has only minor changes. The distance changes are not only caused by the radiosonde drift, but in particular because of the Aeolus measurement grouping algorithm for the measurement selection. As explained in chapter 2 and 5, each profile is one observation with a horizontal length of 90 km, consisting of individual measurements with a horizontal length of about 3 km. Within the observation, the measurements are grouped into the four different classifications, namely $\text{Rayleigh}_{\text{cloudy}}$, $\text{Rayleigh}_{\text{clear}}$, $\text{Mie}_{\text{cloudy}}$ and $\text{Mie}_{\text{clear}}$. As the cloud and aerosol situation is usually not homogeneous within the 90 km, only the measurements which are useful for the respective classification are taken into account. If, for example a cloud layer exists in the first 20 km of the observation, the classification of $\text{Mie}_{\text{cloudy}}$ considers only the measurements of these 20 km. This procedure is not only used for each classification, but is repeated also for each vertical bin. This means, the coordinates of the Aeolus measurements can jump, depending on classification and vertical bin as the centre (middle) of the classification range is given as coordinate. While e.g. at 3 km altitude a cloud is observed for the first 20 km, another one is observed at 7 km altitude in the last 30 km of the 90 km path. Then the coordinates given for 3 km are the mean of the first 20 km, while for 7 km height, the mean of the last 30 km is used.

For the second case study, the point of intersection on 6 December 2018 is chosen, which was west of Namibia (number 6 in Figure 6.3). The radiosonde was launched around 50 km away from the Aeolus overpass, during clear-sky conditions. As the lidar signal in Figure 6.7 shows,

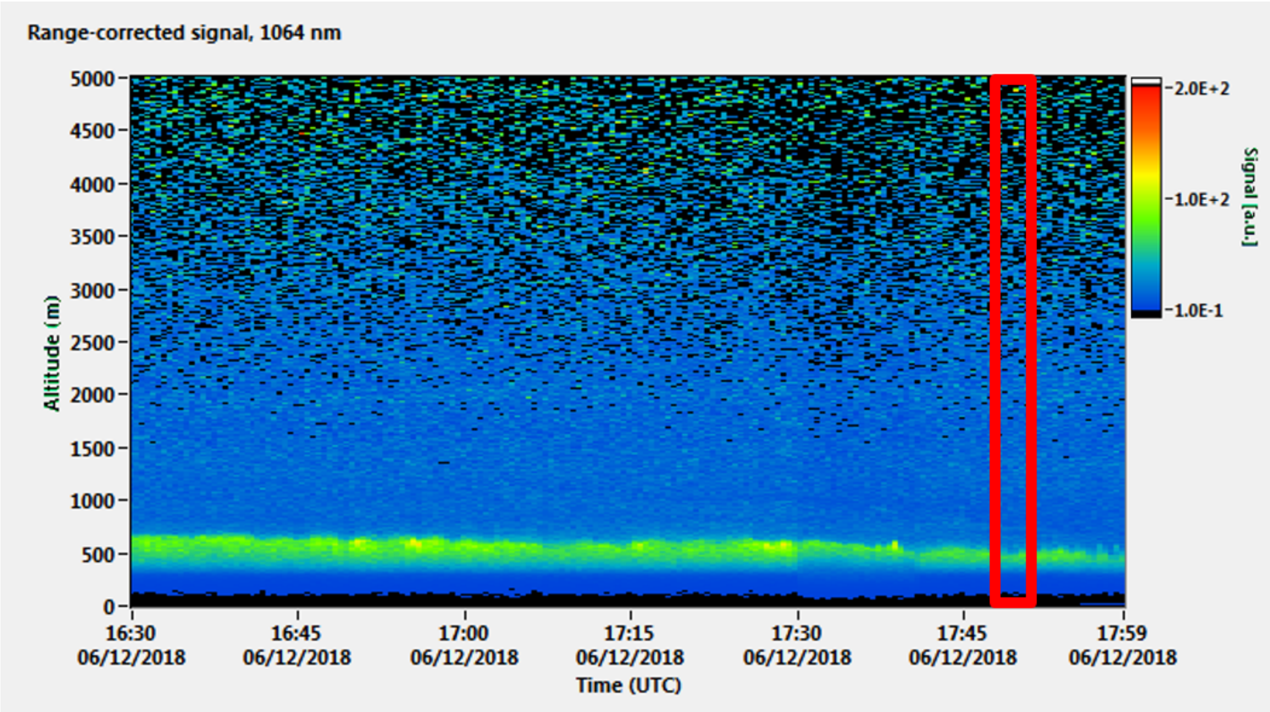

Figure 6.7: The range corrected lidar signal at 1064 nm around the time of the Aeolus overpass (red rectangle) on 6 December 2018.

only a thin aerosol layer existed in the lower 800 m. For this reason, $\text{Mie}_{\text{cloudy}}$ measurements are only expected in low altitudes. Figure 6.8 shows again the radiosonde and Aeolus wind velocity profiles with a high resolved and a low resolved radiosonde profile. As assumed, the $\text{Mie}_{\text{cloudy}}$ measurement only exists for two bins below 930 m, but shows a good agreement with the radiosonde profile. Again, one can see the problem with the low resolution at higher altitudes. Even though the low resolved radiosonde measurements fit with the Aeolus one, the high resolved profile shows much more and stronger changes in wind velocity and direction.
It is interesting in case of the $\text{Rayleigh}_{\text{clear}}$ measurements, that the profile with further distance (blue line) show a better agreement with the radiosonde measurements, than the closer one. It is especially between 7 km to 12 km very similar to the radiosonde profile. However, the mean distance of the two $\text{Rayleigh}_{\text{clear}}$ profiles differs only by ≈ 6 km, which is small compared to the 90 km integration length. Nevertheless, the green profile was measured more southward along the Aeolus track than the blue profile. As it will be described in the following, the overpass was just at the edge of the influence from the Subtropical jet stream, which might be a reason for the stronger west wind component of the more southern Aeolus profile.

As Aeolus overpassed the Polarstern track in the evening, the positive values in the Figure 6.8 indicate westerly winds. Therefore, the profile shows a strong west wind, having its maximum at an altitude of around 10.5 km. Looking at the global atmospheric circulation in Figure 1.2, the point of intersection (number 6 in Figure 6.3) is in the area of the Subtropical jet

(a) High resolution of the radiosonde profile

(b) Low resolution of the radiosonde profile

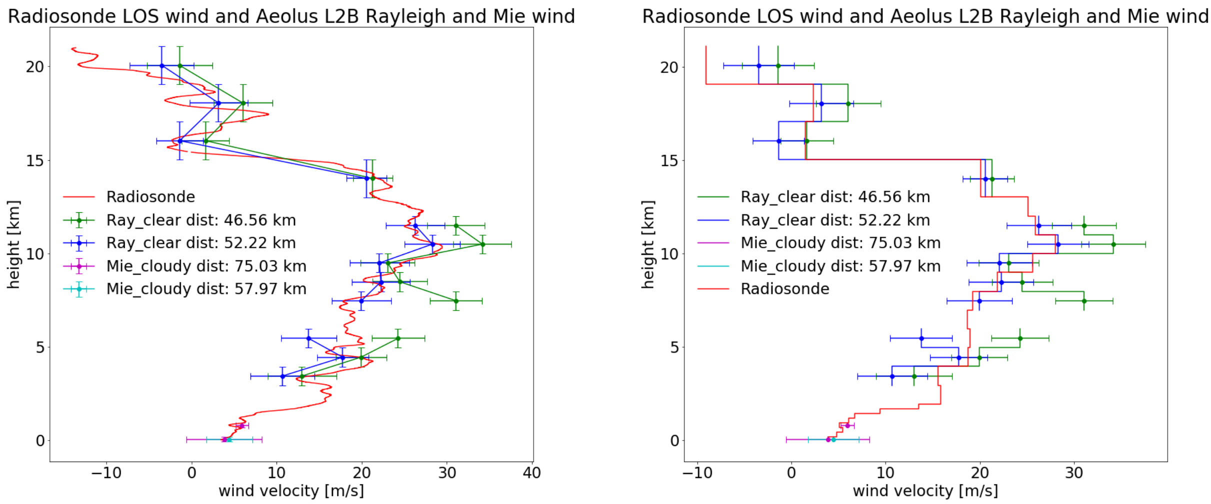

Figure 6.8: Wind velocity profiles measured by the radiosonde (red) with the two closest Aeolus Level 2B (L2B) Rayleigh$_{\text{clear}}$ (green and blue) and Mie$_{\text{cloudy}}$ profiles (magenta and cyan) on 6 December 2018. The radiosonde profile is shown in its highest resolution (a) and with an adjusted resolution to the Aeolus range-bins (b). The radiosonde measurements are projected on the LOS of Aeolus.

stream. To verify this, the Rayleigh$_{\text{clear}}$ HLOS Level 1B wind of the complete orbit of Aeolus, with a length of 90 minutes, is shown in Figure 6.9. The colours indicate whether the wind goes towards (bluish) or away from Aeolus (yellowish). The orbit start just before crossing the North Pole, visible by the strong wind of the Polar vortex in the stratosphere [31]. From the North Pole, Aeolus flies towards the Equator and the South Pole, crossing the Polar and Subtropical jet streams, which are visible by strong negative wind velocities, indicating the west wind. At the South Pole, the colour of the jet streams changes, as Aeolus changes the LOS direction. The light blue line in the Plot presents the time, when Aeolus passed the point of intersection. It is just at the edge of the Subtropical jet.

The four remaining radiosonde wind comparisons with Aeolus of the shipborne validation are shown in Figure 6.10. The numbers in the titles refer to the numbered points of intersection in Figure 6.3. On 27 November 2018 (Figure 6.10 (a)) the mean distances between 134 km to 149 km are just at the very limit of the 150 km radius, which is the threshold value of the distance between radiosonde and Aeolus profile position. It should be mentioned, that the distance of a few range-bins of the Mie$_{\text{cloudy}}$ and Rayleigh$_{\text{clear}}$ profiles are even larger than 150 km. Furthermore, the point of intersection was exactly inside the ITCZ, where enhanced vertical turbulences can occur due to quick changes in local weather. These vertical turbulences cannot be recorded by Aeolus. The Mie$_{\text{cloudy}}$ measurements in altitudes higher

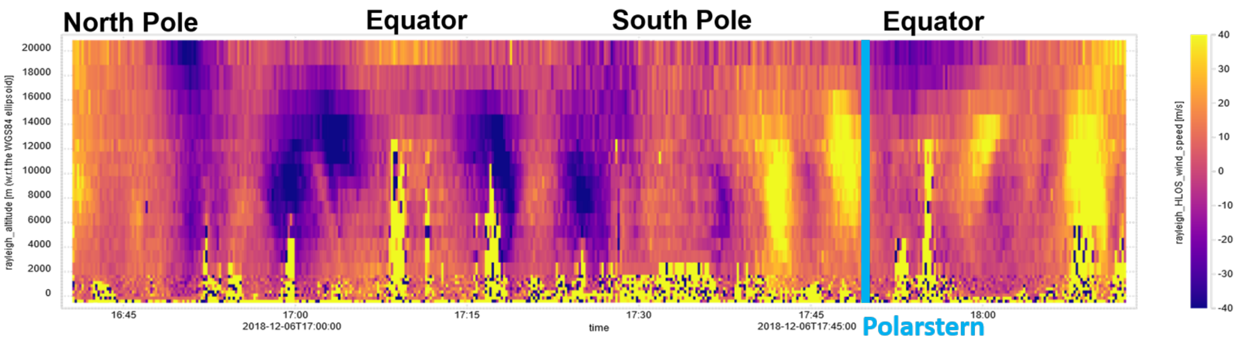

Figure 6.9: Rayleigh$_{\text{clear}}$ Level 1B wind along the whole orbit of Aeolus from 16:40 UTC to 18:12 UTC on 6 December 2018. Negative (bluish) values showing the wind coming towards Aeolus and positive (yellowish) values the wind going away from Aeolus along its LOS. The light blue line shows the time when Aeolus overpassed Polarstern (The Plot was created with the provided VirES interface for Aeolus CAL/VAL teams [32]).

than 10 km show the existence of high clouds. Due to the large horizontal distance between the radiosonde and Aeolus profiles as well as the strong change in local weather with vertical turbulences, it is not surprising, that the Mie$_{\text{cloudy}}$ measurements differ stronger than in the two case studies. Also one of the Rayleigh$_{\text{clear}}$ bins at 14 km is totally out of range. With the given information it is not possible to prove, if the wind really changes that strong or if Aeolus measures the wind incorrectly at that bin.

Also the next point of intersection, that took place on 2 December 2018 (Figure 6.10 (b)), has high mean distances between 100 km to 122 km. The radiosonde profile shows a stronger fluctuation of the wind velocity and direction than in the already discussed case studies. Figure 6.11 shows the wind direction of the radiosonde for that profile. It shows large and fast changes and between 5 km to 16 km no strong east or west component of the wind. Besides the horizontal distance, this might be an additional reason for stronger deviations of the Aeolus profiles.

While the mean distances during the point of intersection on 3 December 2018 (Figure 6.10 (c)) have for all Aeolus profiles less than 100 km, the last point of intersection on 10 December 2018 (Figure 6.10 (d)) was again more than 100 km away. Like in the second case study, the Rayleigh$_{\text{clear}}$ profile, which was further away is partly in better agreement with the radiosonde profile, than the closer one.

(a) 27 November 2018, Nr. 2

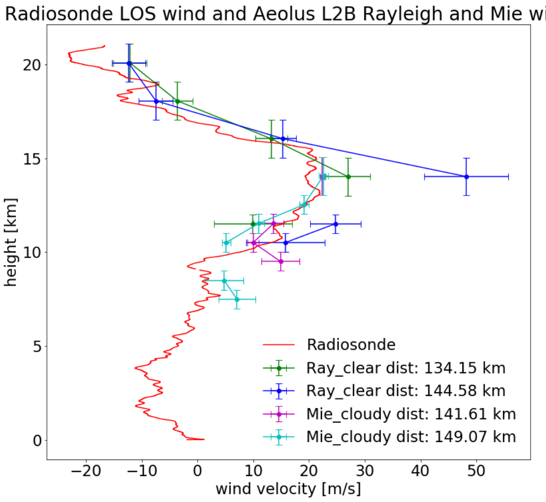

(b) 2 December 2018, Nr. 4

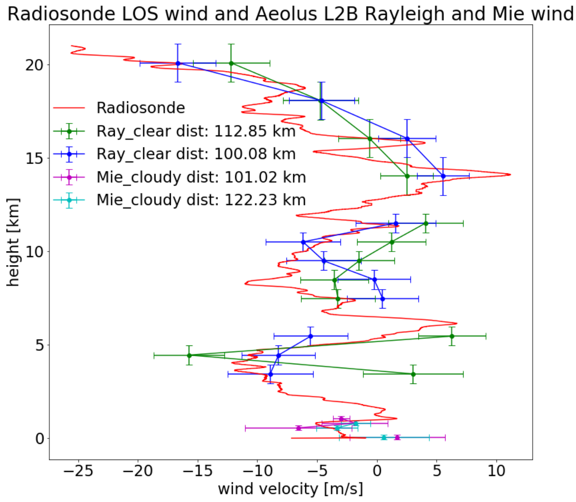

(c) 3 December 2018, Nr. 5

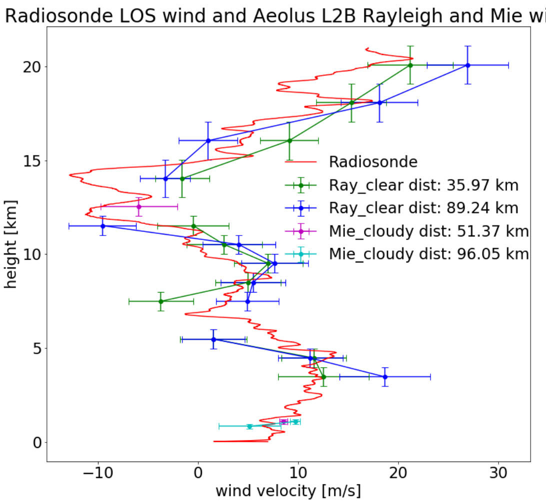

(d) 10 December 2018, Nr. 7

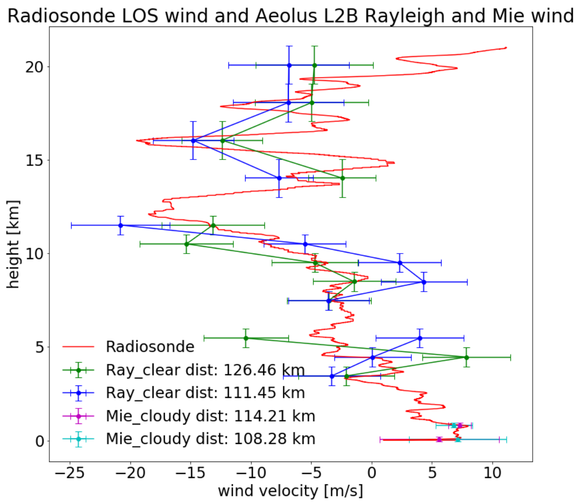

Figure 6.10: Wind velocity profiles measured by the radiosonde (red) with the two closest Aeolus Level 2B (L2B) Rayleigh$_{\text{clear}}$ (green and blue) and Mie$_{\text{cloudy}}$ profiles (magenta and cyan) of all remaining comparisons during the Polarstern cruise. The numbers in the titles refer to the numbered points of intersection in Figure 6.3.

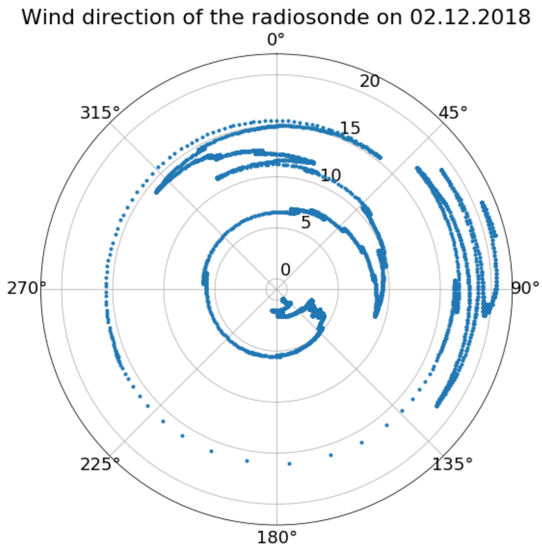

Figure 6.11: The wind direction measured the radiosonde on 2 December 2018.

Statistics

In this subsection, the performed comparisons are analysed statistically. Of special interest are the biases and coefficients of determination and correlations for the $\mathrm{Rayleigh}_{\mathrm{clear}}$ and $\mathrm{Mie}_{\mathrm{cloudy}}$ profiles, as these parameters were mainly discussed during the first Aeolus CAL/VAL workshop [22] and are used as performance indicator of Aeolus.

Starting with the $\mathrm{Rayleigh}_{\mathrm{clear}}$ wind, all measurements of each range-bin are plotted against the low resolved values of the radiosondes in Figure 6.12 (a), to obtain a reasonable evaluation with respect to the instrument performance. Figure 6.12 (b) shows the normalized frequency distribution of the deviation between the $\mathrm{Rayleigh}_{\mathrm{clear}}$ and radiosonde wind measurements. As it is not clear if the wind value at 14 km of 27 November 2018 represents the actual wind situation, this measurement is excluded from the calculations. The trend line has a gradient of 0.97 with a bias of 1.77 ms^{-1}. The calculated bias confirms the observation made in the first case study. On the Aeolus CAL/VAL workshop [22], other CAL/VAL teams reported biases in the same range between < 1 ms^{-1} to 3.3 ms^{-1}. Global biases of around 2 ms^{-1} were found for example at comparisons[1] with the Météo-France NWP model as well as with the ECMWF model.

Furthermore, the calculated coefficient of determination is $R^2 \approx 0.862$. Its square root results in the correlation coefficient:

$$r = \sqrt{R^2} \approx 0.928 = 92.8\% \tag{6.2}$$

[1] not publically accessible

(a) Rayleigh$_{clear}$ Level 2B wind vs. radiosonde wind

(b) Normalized frequency distribution of the deviation

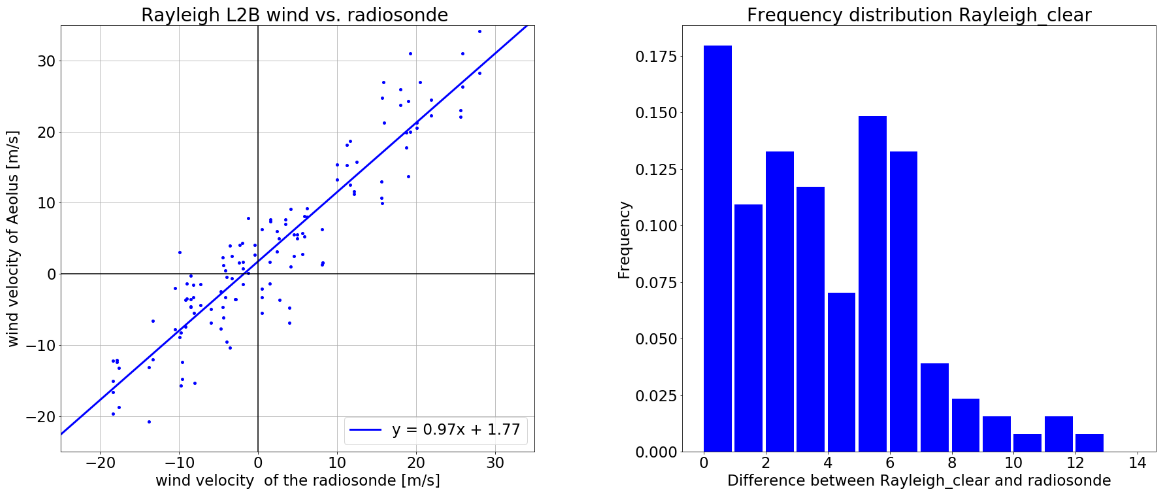

Figure 6.12: The Rayleigh$_{clear}$ wind vs. the radiosonde measurements (a) of all measurements made during the shipborne validation. Only the Rayleigh$_{clear}$ bin with the extreme deviation of 27 November 2018 is excluded. The normalized distribution of the deviation (b).

For November and December a correlation coefficient between 95% to 96% with the ECMWF model for all global observations was calculated, as reported on the Aeolus CAL/VAL workshop [22]. Considering the small number of measurements in this validation, the correlations are still in good agreement.

For the normalized frequency distribution of the difference between the Aeolus and the radiosonde measurements in Figure 6.12(b), the low resolved radiosonde data were used. In most cases, the Plot shows a deviation below 7 ms^{-1}. Even though it seems to be quite large, this is a reasonable result, taking the following aspects into account: First of all, this validation considers all Aeolus measurements with an uncertainty lower than 8 ms^{-1}. Furthermore the Aeolus measurements have the bias of 1.77 ms^{-1}, which increases the deviation. Last but not least, Aeolus has a horizontal resolution of 90 km, while the radiosonde is only a point measurement and the deviation caused by the horizontal distance between radiosonde and Aeolus profile must be considered as well.

The results of the Mie$_{cloudy}$ comparisons are shown in Figure 6.13. Plot (a) and (b) consider all measurements, Plot (c) and (d) exclude the 27 November 2018.

The statistics of all measured Mie$_{cloudy}$ profiles have a bias of 1.77 ms^{-1} and a correlation coefficient of 79.2 %. If one exclude the 27 November 2018, the correlation increases strongly. Then, the measurements correlate with 91.5%, having a bias of only 0.52 ms^{-1}. Also the frequency distribution shows a better result, by excluding that day. While Figure 6.13 (b) shows

(a) $\text{Mie}_{\text{cloudy}}$ Level 2B wind vs. radiosonde wind with the measurements of 27 November 2018

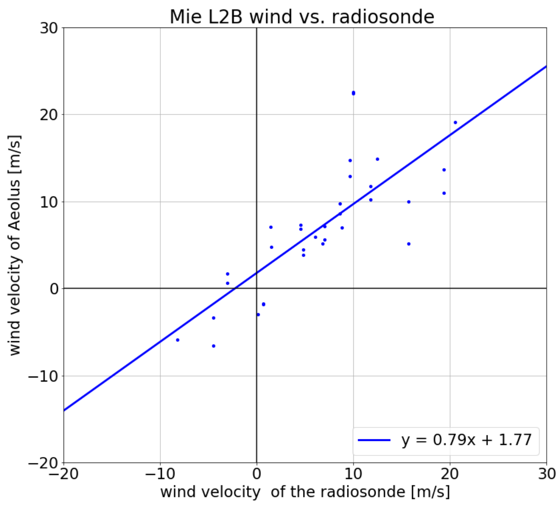

(b) Normalized frequency distribution of the deviation with the measurements of 27 November 2018

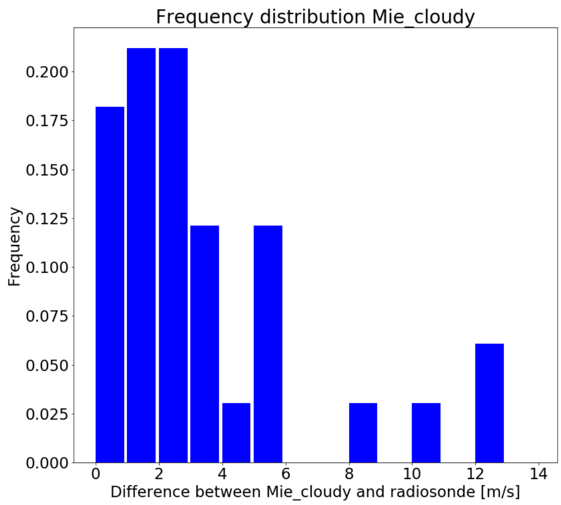

(c) $\text{Mie}_{\text{cloudy}}$ Level 2B wind vs. radiosonde wind without the measurements of 27 November 2018

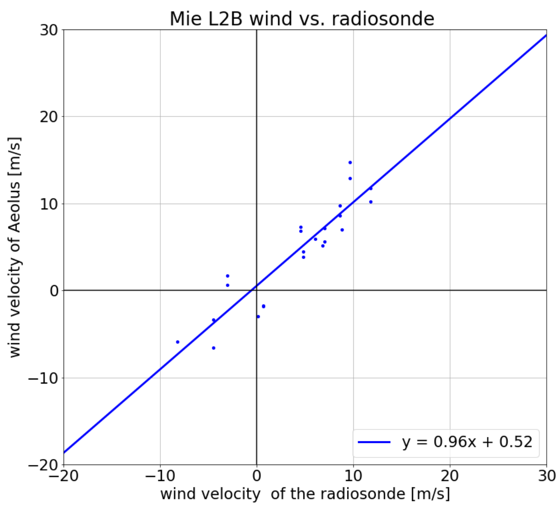

(d) Normalized frequency distribution of the deviation without the measurements of 27 November 2018

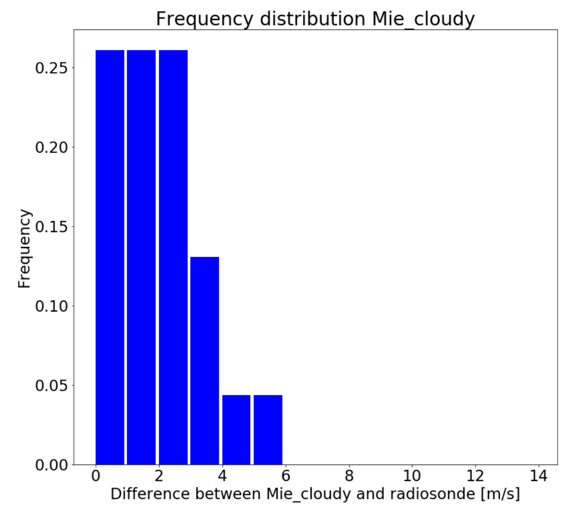

Figure 6.13: All $\text{Mie}_{\text{cloudy}}$ wind measurements vs. the radiosonde measurements from the shipborne validation and the normalized distribution of their deviation with the comparison of 27 November 2018 (a, b) and without it (c,d).

deviations higher than 12 ms^{-1}, all deviations are below 6 ms^{-1} in Figure 6.13 (d). In this statistic it is clearly shown that the comparison on 27 November 2018 does not represent the quality of the Mie_{cloudy} measurements. This is caused by the high horizontal distance, which has especially large effects inside the ITCZ, having strong upward drifts and quick changes in local weather.
Considering the frequency distributions, the Mie_{cloudy} profiles show less deviation than the $Rayleigh_{clear}$ profiles. This tendency fits with the reported random errors of the $Rayleigh_{clear}$ (≈ 4 ms^{-1}) and the Mie_{cloudy} measurements (≈ 2.5 ms^{-1}), as discussed in chapter 4. On the Aeolus CAL/VAL workshop [22] and in internal summary reports[1] the reasons for the different errors were assumed to be the lower measured Rayleigh return signal and the lower laser energy. As the Rayleigh scattering is orders of magnitude lower than the Mie scattering, the lower laser energy affects the Rayleigh measurements stronger.

To summarize, the statistics fit with the internal reported observations of other CAL/VAL teams and gives a good insight into the performance of Aeolus. The appearing differences are caused by the different validation conditions, like a small number of comparisons in this statistic, a large tolerated horizontal distance between radiosonde and Aeolus as well as the spatial limitation on the Atlantic Ocean in the tropical and subtropical regions.

6.1.2 Aerosol validation

As additional spin-off product, Aeolus delivers also aerosol properties. Thus comparisons with respect to these properties are shown. During the Polarstern cruise, two cases were available for comparisons. One was during the days of 25 November 2018 to 26 November 2018 in the area of West Africa, where Polarstern passed a dust layer and the other one was at the point of intersection on 29 November 2018. For the comparisons, the Level 2A aerosol prototype-product (see chapter 5) of Aeolus is used. The Aeolus aerosol product is compared to the measurements, performed with the $Polly^{XT}$ lidar on board of Polarstern.

Figure 6.14 shows the near field of the uncalibrated attenuated particle backscatter coefficient for the wavelength of 532 nm (upper Plot), measured by the $Polly^{XT}$ lidar. The lower Plot shows the volume depolarization ratio for the wavelength of 532 nm between 23 November 2018 and 27 November 2018. As one can see in the lower Plot, the depolarization ratio increases strongly on 25 November 2018 and decreases slowly again during the 27 November 2018. The predicted dust concentration in that area for the 25 November 2018 at 12 UTC is shown in Figure 6.15. The dust prediction is provided by the SKIRON weather forecast system of the Atmospheric Modeling and Weather Forecasting Group from the University of Athens [33, 34]. The red triangle illustrates the position of Polarstern at that time. Aeolus had two overpasses

[1] not publically accessible

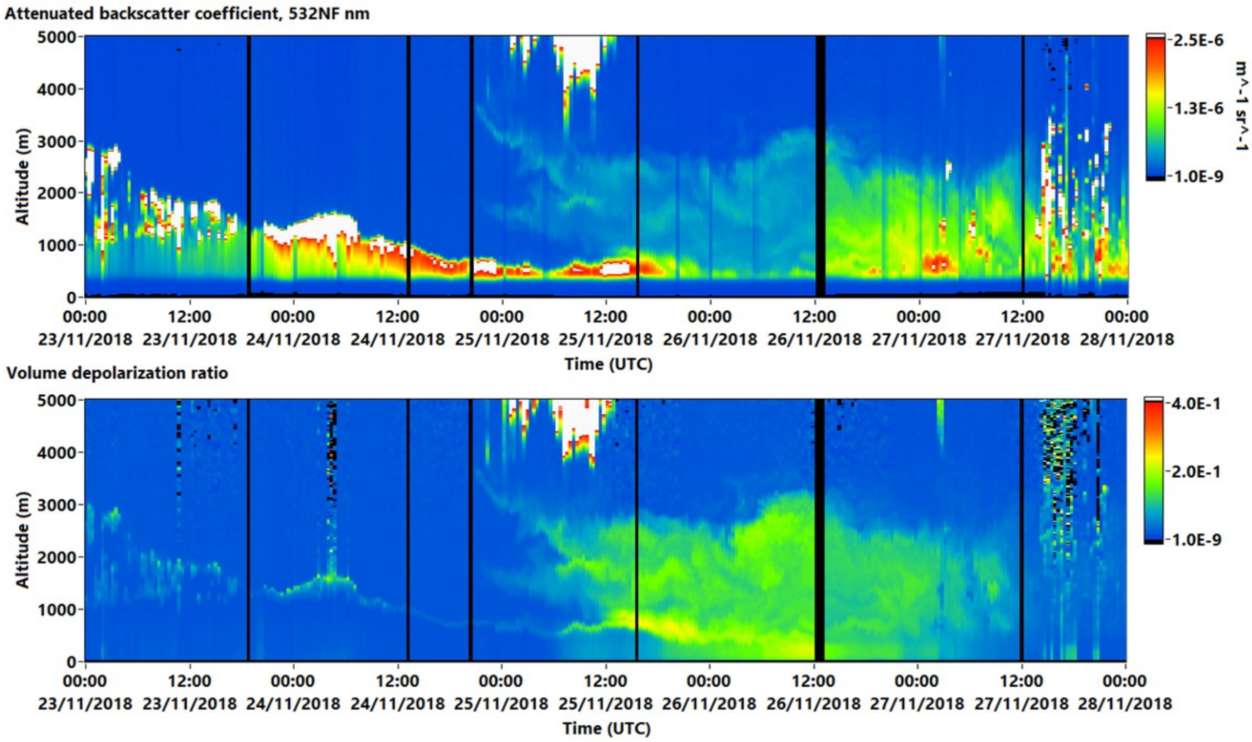

Figure 6.14: Measurements of the Polly^{XT} lidar. Near field of the uncalibrated attenuated particle backscatter coefficient (upper Plot) and the uncalibrated volume depolarization ratio (lower Plot) for the wavelength of 532 nm and between 23 November 2018 and 27 November 2018.

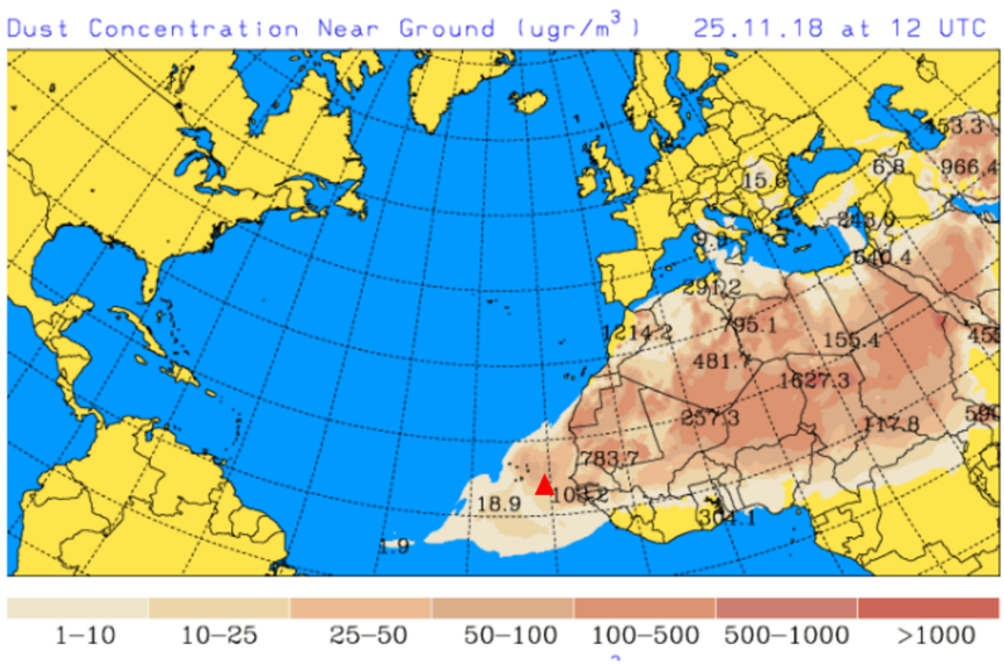

Figure 6.15: Predicted dust concentration near ground [μgr/m^3] on 25 November 2018 at 12 UTC. The red triangle shows the position of Polarstern at that moment (The prediction was taken from the provided SKIRON forecast system of the University of Athens [33, 34]).

in that area, one on Sunday morning the, 25 November 2018 and one on Monday morning, 26 November 2018. Unfortunately, Polarstern couldn't reach the overpasses within a 150 km radius, which is why no radiosonde was launched. But as seen in the predicted dust concentration and the depolarization ratio, the dust layer covers a large area of the West African coast. For the comparison, the overpass of Aeolus on 25 November 2018 is compared with the Polly^{XT} lidar analysis on 26 November 2018 between 00 UTC to 06 UTC. Even though the position is not the same, Aeolus should measure a similar dust layer as the Polly^{XT} lidar.
For the comparison, the particle backscatter coefficient (Figure 6.16 (a)), the particle extinction coefficient (Figure 6.16 (b)), and the lidar ratio (Figure 6.16 (c)) of the Polly^{XT} lidar and the Aeolus measurements are plotted. The Aeolus Level 2A product provides amongst others two different profiles. The red one is called Standard Correct Algorithm (SCA), containing all variances of SCA products per range-bin and the green is called SCA mid bin, made from two

(a) Backscatter coefficient

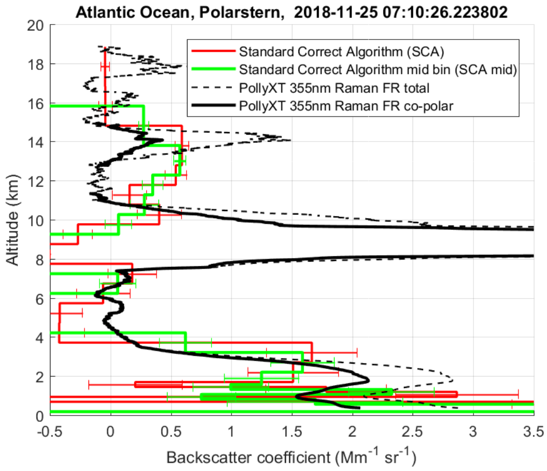

(b) Extinction coefficient

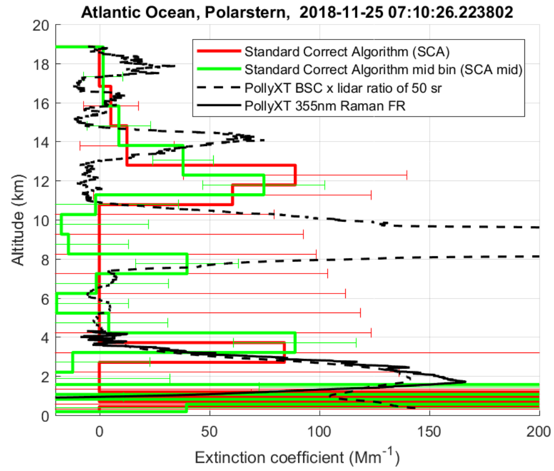

(c) Lidar ratio

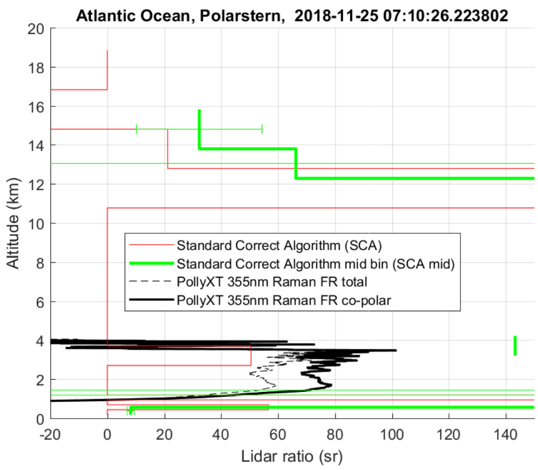

Figure 6.16: Comparison of Aeolus and Polly^{XT} particle backscatter coefficient (a), the particle extinction coefficient (b) and the lidar ratio (c) on 25 November 2018 (Plots created by Holger Baars).

halves of neighbouring Rayleigh range-bins [13, 35]. The Polly^{XT} lidar measurements are subdivided into the particle backscatter coefficient and lidar ratio of the total Raman signal (black solid line) and only the co-polar Raman signal (black dotted line) at 355 nm. The particle extinction coefficient is calculated one time with the Raman method (solid line) and the other one by multiplying the particle backscatter coefficient with an assumed lidar ratio of 50 sr (dotted line), which is the typical range of lidar ratios for dust layers [17]. As ALADIN has the same transmitter and receiver telescope, it can measure only the co-polar component of the backscattered light (see section 3.5), which is why also only the co-polar component of the Polly^{XT} lidar measurements is plotted.

The Polly^{XT} lidar measurements show in Figure 6.16 (a) an increase of the particle backscatter coefficient up to an altitude of 4 km. The increase is caused by the dust layer in this area. Furthermore a cloud layer is measured, indicated by the strong particle backscatter coefficient between the heights of 8 km to 10 km. While Aeolus receives a very noisy particle backscatter signal in the range up to 2 km, it measures a similar particle backscatter coefficient between 2 km and 4 km, like the Polly^{XT} lidar. Above the 4 km, the measurements are mainly negative, besides two more increases of the particle backscatter coefficient in the heights of 6 km to 8 km and of 10 km to 16 km. This disagrees with the Polly^{XT} lidar measurements, but is not surprisingly, as the measurements were made at different times and positions. Thus, the cloud layers differ. Important is, that the Polly^{XT} lidar as well as Aeolus measures both a layer between 2 km and 4 km.

Regarding the particle extinction coefficient in Figure 6.16 (b), the Aeolus measurements are again very noisy in the first 2 km. Between the altitudes of about 2.8 km and 4.2 km, Aeolus measures a particle extinction coefficient of about 80 Mm^{-1} to 85 Mm^{-1}. The signal seems to be shifted upwards compared to the particle extinction coefficient measured by the Polly^{XT} lidar.

For the lidar ratio in Figure 6.16 (c), the signals of Aeolus are very few and rather noisy up to the height of 4 km. While the SCA mid bin has only one very high measurement of more than 140 sr between the height of 3 km to 4 km, the SCA profile shows at least one measurement at around 50 sr in this range. This value is lower compared to the co-polar measurement of the Polly^{XT} lidar, which has a lidar ratio at about 75 sr.

In summary, the comparison shows, that Aeolus could recognize an aerosol layer in the same altitude as the Polly^{XT} lidar. However, it is not possible to characterize the observed layer from the measured optical properties and shows that the aerosol products of Aeolus are not yet fully exploited.

For the second case study the measurement on 29 November 2018 was chosen. Polarstern could reach the point of intersection with the Aeolus overpass within a radius of about 30 km. Figure 6.17 shows an extract of the measured aerosol product along the Aeolus track, using the extinction product from the Mie channel algorithm (MCA). This algorithm provides only particulate extinction and needs therefore priori information on the lidar ratio. It is taken from the auxiliary climatological datasets, which are based on other space-borne lidar measurements [13, 23]. However, this is only a crude estimation of the lidar ratios and leads to highly biased MCA profiles. Still, it gives a good overview of the existing aerosol and cloud layers. The red triangle marks the position of Polarstern at the time of the overpass. Looking at the stronger signals in the extract, a layer in the lower range-bins is observed around Polarstern. Turning more to the continent, more signals in the higher altitudes appear, which is an indication for cloud occurrence.

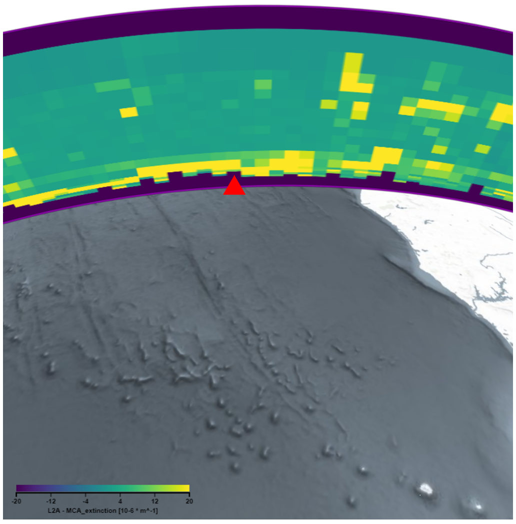

Figure 6.17: Extract of the measured Level 2A MCA extinction coefficient along the track of Aeolus, overpassing the Polarstern cruise on 29 November 2018. The red triangle marks the position of Polarstern (The Plot was created with the provided VirES interface for Aeolus CAL/VAL teams [32]).

Zooming to the point of intersection, Figure 6.18 shows the comparison of the Polly^{XT} lidar and the Aeolus measurements up to an altitude of 8 km. For the lidar signal, a cloud free time period is chosen between 03:10 UTC to 03:50 UTC to cover the complete height of the aerosol layer. The particle backscatter coefficients of the Aeolus measurements in Figure 6.18 (a) is very high in the lower 2 km. As seen before in the lidar signal of that day (Figure 6.4), a cloud layer existed at the time of the overpass at 2 km. The high particle backscatter coefficient might indicate the cloud. Above, between 2 km to 5 km the coefficient is in good agreement with the Polly^{XT} lidar measurements. Both are measuring a similar particle backscatter coefficient in that altitude. Regarding the particle extinction coefficient (Figure 6.18 (b)), the Aeolus measurements show very high values in the first 2 km. It is either caused by the cloud or is in general very noisy. Above, especially the SCA profile have a higher coefficient in the same altitude as the Polly^{XT} lidar measurements, but a large estimated error bar. The lidar ratio (Figure 6.18 (c)) has between the altitudes of 2 km and 4 km values at 15 sr to 60 sr for the Aeolus profiles, while the Polly^{XT} lidar measures a ratio of around 75 sr for the co-

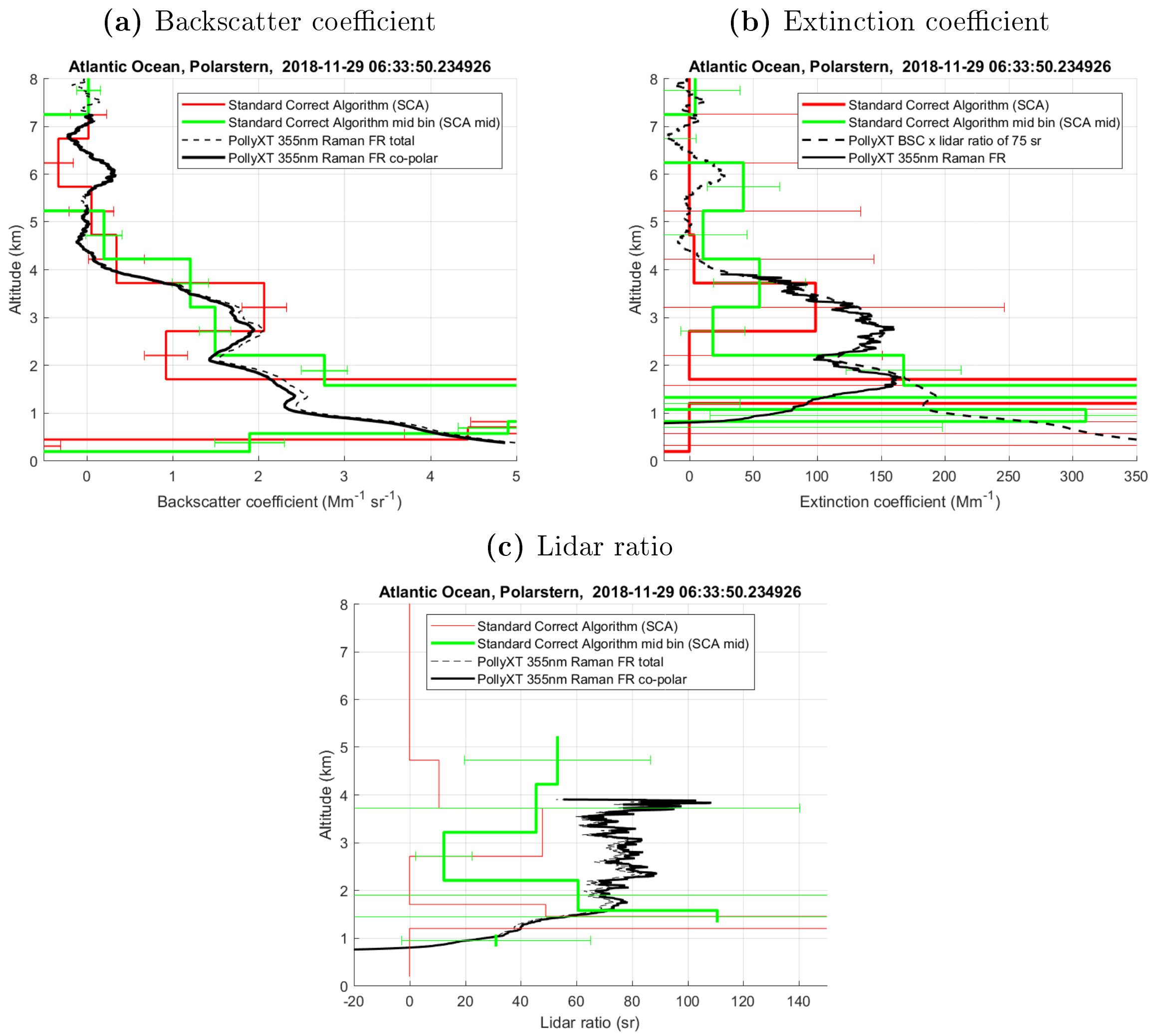

Figure 6.18: Comparison of Aeolus and Polly^{XT} lidar particle backscatter coefficient (a), the particle extinction coefficient (b) and the lidar ratio (c) on 29 November 2018 (Plots created by Holger Baars).

polar component and for the total signal. Like in the first case study, Aeolus does recognize a layer in the same altitude as the Polly^{XT} lidar measurement, showing both a similar particle backscatter coefficient. Even though measurements of the particle extinction coefficient and the lidar ratio are better than in the first comparison, it is still not possible to characterize the layer clearly.

In general, several reasons complicate the characterization: Due to the instrumental setup of ALADIN, only the co-polar component is measurable. This leads to an underestimation of the particle backscatter coefficient and therefore an overestimation of the lidar ratio for high depolarizing aerosol/ice particles (see section 3.5). Besides this limitation, the algorithm of the Level 2A aerosol product assumes furthermore a homogeneous particle filling of the range-bins [13]. But the aerosol and cloud layers are rarely homogeneous within the 90 km observation

length of the Aeolus profiles. Furthermore, high cloud layers are influencing the measurements below the cloud, as the signals attenuate caused by multiple scattering within the cloud.
The focus of this Master thesis lies on the wind validation, but these two case studies shall give an insight of the aerosol products of Aeolus. For a proper statement and statistic of its quality and problems, more comparisons with high and clear characterized aerosol layers need to be done. For this the PollyNET ground stations of TROPOS [36], especially the ones that are in dust areas, are useful for Aeolus validation and calibration.

6.2 Land-based validation

Besides the shipborne wind and aerosol validation, a supplementary land-based wind validation was performed, using Leipzig as ground station. Aeolus is overpassing Leipzig twice a week, one time on Friday evening with a distance of about 20 km and one time on Sunday morning with a distance of about 40 km. For the validation of the wind profiles, radiosondes are launched each Friday, starting in mid May 2019. The launches are performed at TROPOS with the Vaisala sounding system MW41 [37], using the radiosonde types RS92 and RS41 [29, 27]. The different radiosonde types do not differ in the quality of wind measurements, as both are using the same technique to derive wind velocity and direction [30]. As performed in the shipborne wind validation, the radiosondes wind profiles are compared to the Aeolus Rayleigh$_{\text{clear}}$ and Mie$_{\text{cloudy}}$ wind profiles. In this thesis only the overpasses between 17 May 2019 and 14 June 2019 are considered. This is because the laser was switched to the second laser of ALADIN on 16 June 2019, due to the strong decrease of the emitting laser energy of the first laser. As it takes a while, until all Aeolus products are correctly calibrated with the new laser, measurements with the second laser are not included here.

Case studies and statistics

During the validation period between 17 May 2019 and 14 June 2019, five radiosondes could be launched. As case study the comparison, measured on 31 May 2019 is chosen and shown in Figure 6.19. Plot (a) shows the wind velocity of the high resolved radiosonde profile with the Aeolus profiles along the LOS and Plot (b) the wind direction of the radiosonde profile during the ascent. The wind measurements of Aeolus and the radiosonde differ much more, compared to the discussed cases of the shipborne validation. They do not only deviate stronger in wind velocities, but have also different signs, which means they also disagree in the wind directions. Furthermore the error bars are large, especially for the Rayleigh$_{\text{clear}}$ profiles. They are close to 8 ms^{-1}, which is the error threshold in this thesis, as defined in the data filtering (see chapter 5).
For the explanation of the declined quality of the Aeolus wind measurements, several reasons need to be considered: First of all, the variation of wind velocity within a horizontal resolution

(a) Radiosonde and Aeolus wind profiles

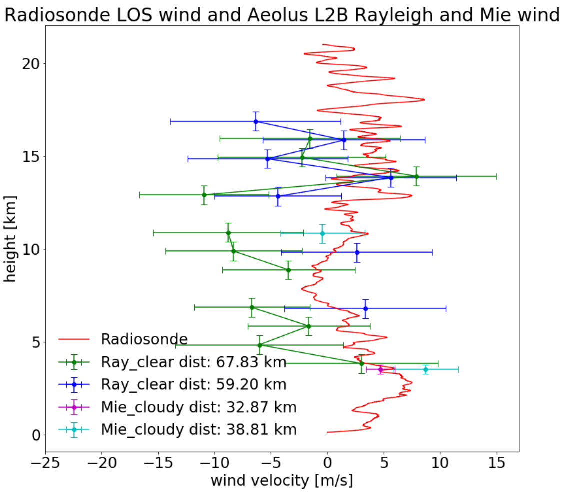

(b) Wind direction

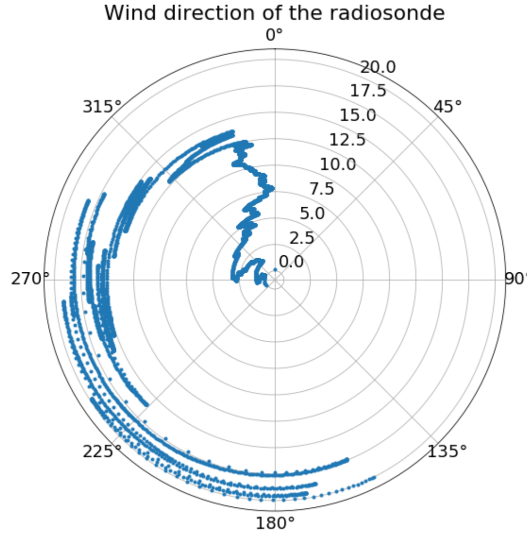

Figure 6.19: Wind velocity profiles measured by the radiosonde (red) with the two closest Aeolus Rayleigh$_{clear}$ (green and blue) and Mie$_{cloudy}$ profiles (magenta and cyan) on 31 May 2019 in Leipzig (a). The wind direction of the radiosonde profile (b). The radius of the circles in (b) denotes the altitude in kilometre.

of 90 km is in general stronger above the land compared to the open ocean, as the wind is influenced by the orography along the LOS, having more turbulences, primary in the PBL. Though it should be mentioned, that the horizontal resolution of the Mie channel was increased to around 10 km on 5 March 2019. Also the vertical resolution was increased compared to the one of the Rayleigh measurements, having now a vertical resolution of 250 m up to ≈ 1.32 km, 500 m between ≈ 1.32 km and ≈ 5.35 km and 1 km between ≈ 5.35 km to ≈ 16.5 km.

The Mie$_{cloudy}$ profiles have two cyan and one magenta coloured wind measurements in Figure 6.19 (a). They show better results than the Rayleigh$_{clear}$ wind values, but only the magenta measurement is in really good agreement with the radiosonde wind profile.

Furthermore the weekly data quality report[1] for the CAL/VAL teams records an observed Observation minus Background (O−B) standard deviation (with *background* a reference measurement is meant, that uses the short-range forecast from the ECMWF model) of more than 7 ms^{-1} for the Rayleigh$_{clear}$ measurements for the measurement period of the land-based validation. During the period of the Polarstern validation the O−B standard deviation of the Rayleigh$_{clear}$ measurements were still at around 4.5 ms^{-1}, as it is reported in the Aeolus summary report[1] of the first three months. The reason for the high value is assumed to be a combination of increased solar background noise in the Northern Hemisphere, an increase in hot pixel associated noise, as well as the decrease in laser energy with time. At the time of the overpass, the laser energy was only at 42 mJ. During the shipborne validation, the emitted

[1] not publically accessible

laser energy was still about 55 mJ.
Another reason is the wind direction on that day. Plot 6.19 (b) shows that the wind had a strong northerly component between 5 km to 13.5 km. This leads to a projected wind velocity along the LOS close to 0 ms^{-1}. In other words, at small wind velocities the Aeolus wind direction can change, but stays in the range of the standard deviation. Another point is that the random and systematic error stays constant compared to high west-east wind velocities. With a high range of wind velocity, the measurements have a better correlation with the same error estimation than having a low range of wind velocity at around 0 ms^{-1}, where the error estimation has the same range or even higher than the wind velocity itself.

The overview of all remaining radiosonde and Aeolus wind profiles of the land-based validation in Leipzig are shown in Figure 6.20. Like in the discussed case study, the estimated error

(a) 17 May 2019

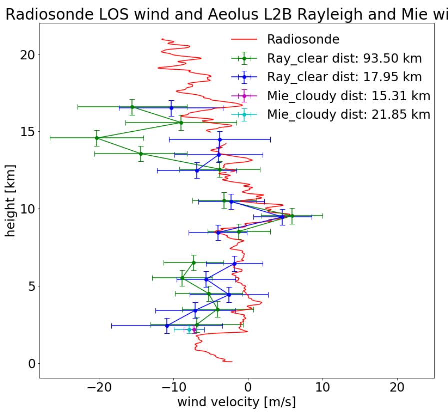

(b) 24 May 2019

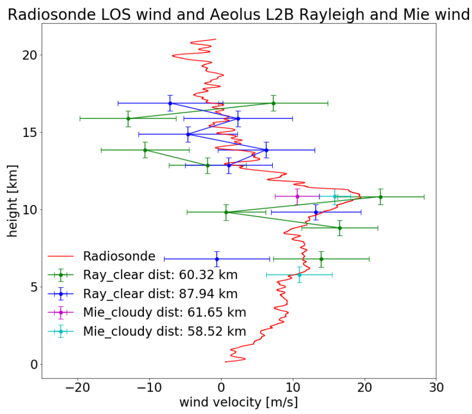

(c) 7 June 2019

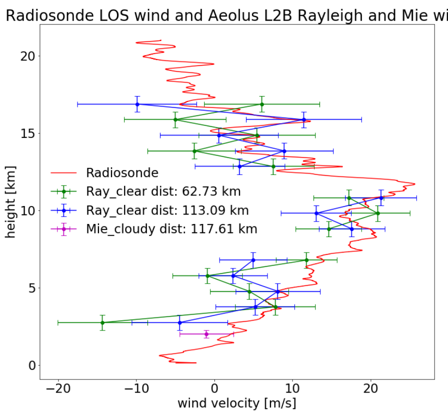

(d) 14 June 2019

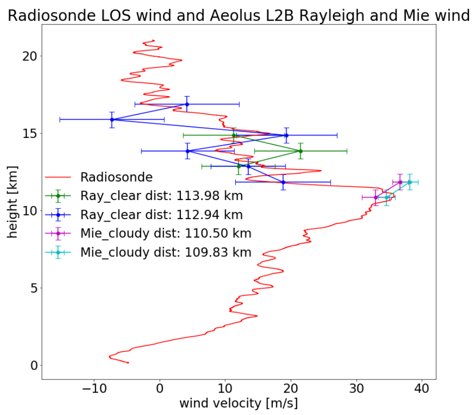

Figure 6.20: All remaining wind velocity profiles of the land-based validation in Leipzig, measured by the radiosondes (red) and the two closest Aeolus Rayleigh$_{clear}$ (green and blue) and Mie$_{cloudy}$ profiles (magenta and cyan).

is much larger than in the comparisons of the wind profiles, measured during the Polarstern cruise. Furthermore it seems that more outliers with a deviation higher than 10 km exist. This is verified in Figure 6.21, which shows the wind measurements of Rayleigh$_{\text{clear}}$ plotted against the radiosondes (Plot (a)) and the normalized frequency distribution of their deviation (Plot (b)). The linear regression has a gradient of 1.07 with a negative bias of -4.36 ms^{-1}. As written in chapter 4, the hot pixel correction was implemented on 14 June 2019, which means it is already included in the last comparison. But as the Rayleigh$_{\text{clear}}$ signal could not penetrate the high clouds on this day, the correction leads only to one additional Rayleigh$_{\text{clear}}$ and Mie$_{\text{cloudy}}$ range-bin. Still, when considering the additional bin, the Rayleigh$_{\text{clear}}$ measurement correlation increases from 77.1% to 78.1%. Conspicuous is, that this time the comparison results in a

(a) Rayleigh$_{\text{clear}}$ wind vs. radiosonde wind

(b) Normalized frequency distribution of the deviation

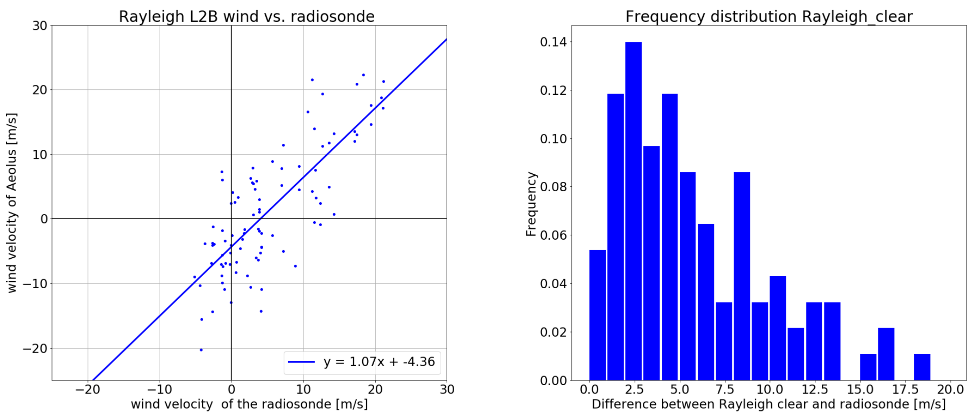

Figure 6.21: The Aeolus Rayleigh$_{\text{clear}}$ wind velocity vs. the radiosonde wind measurements in Leipzig between the period from 17 May 2019 to 14 June 2019 (a). The normalized distribution of the deviation between the Aeolus Rayleigh$_{\text{clear}}$ wind velocity and the radiosonde wind measurements, that were adjusted to the same resolution as the Aeolus measurements (b).

negative and larger bias and not in a positive one like in the shipborne validation. This is also observed and discussed in the weekly quality reports[1] for the CAL/VAL teams. In the report, the Rayleigh$_{\text{clear}}$ latitude depending bias of the ascending orbit (upper Plot of Figure 6.22) and the descending orbit (lower Plot of Figure 6.22) for the time period between mid April 2019 to mid June 2019 is shown. A significant bias change was observed after updating the processing chain on 16 May 2019. While the global average bias was improved by about 3 ms^{-1}, the bias of the Northern mid latitudes and polar region started to get negative. The strength of the bias differs also depending on the descending or ascending orbit. As the land-based validation started at the 17 May 2019, all comparisons of the land-based statistic include the new bias.

[1] not publically accessible

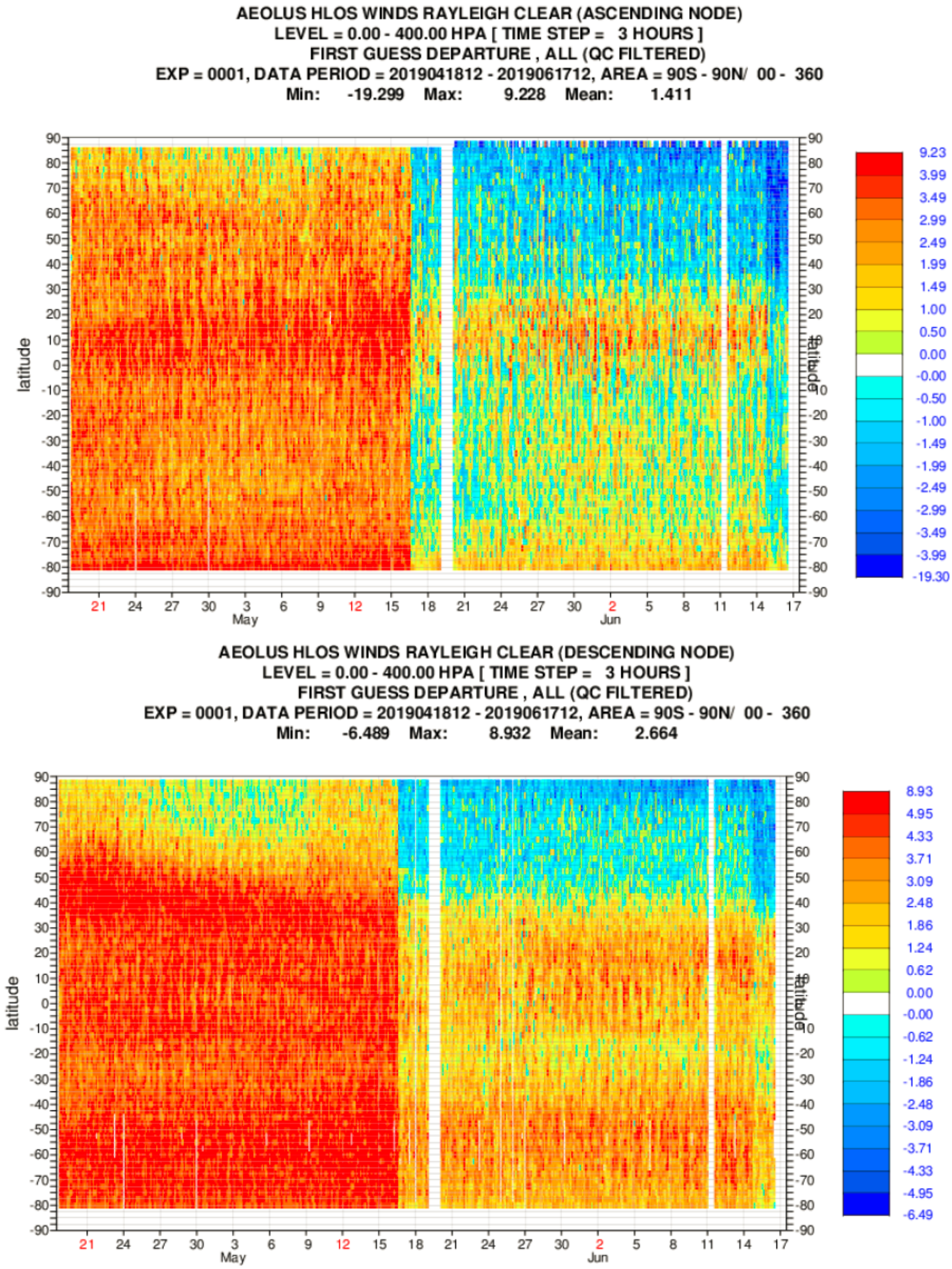

Figure 6.22: Rayleigh$_{\text{clear}}$ latitude depending bias of the ascending orbit (upper Plot) and the descending orbit (lower Plot) for the time period of mid April 2019 to mid June 2019 (The Plot is taken from the weekly quality reports, accessible for the CAL/VAL teams).

The normalized frequency distribution in Plot 6.21 (b) shows several deviations with even more than 15 ms^{-1} (without subtracting the calculated bias from the Aeolus measurements). The statistic shows a stronger deviation of the measured values, than in the shipborne validation. An important reason for this is the low emitting laser energy. With the higher and more stable energy of the second laser as well as the implemented hot pixel correction, the quality of the Aeolus wind measurements should increase significantly in future. Furthermore the data will be further reprocessed and improved in the frame of the ACVT, the Aeolus DISC and the SAG, also including the results of the continuously validations and calibrations of the different CAL/VAL teams.

7 Summary and conclusion

In this Master thesis, the wind and aerosol products recorded by the recently started satellite Aeolus were compared to vertical wind and aerosol profiles from radiosonde launches and lidar measurements with the Polly^{XT} lidar during the shipborne validation across the Atlantic Ocean and the land-based validation at Leipzig.
Aeolus enables a completely new dimension for the assimilation of global wind observations in NWP models. With its new technology, Aeolus is the first Doppler wind lidar operating from space and providing global horizontal wind measurements within an altitude range of 0 km to 30 km. The instrument on board is a high spectral resolution lidar, called ALADIN. It measures the Doppler shift at moving molecules and particles, separately in two different receiver channels, the Rayleigh and Mie channel. Besides wind profiles, Aeolus can obtain the lidar ratio by measuring the particle backscatter and particle extinction coefficient independently. However, the aerosol and cloud classification is limited by the fact that Aeolus only transmits the co-polarized component of the backscattered light.
To control the quality of the wind and aerosol profiles, validations and calibrations are made with NWP models and with measurements, performed by radiosondes, balloons, satellites, aircraft, and ground-based instruments.
An unique opportunity was offered by the Polarstern cruise PS116 in Autumn 2018 to perform shipborne validation across the Atlantic Ocean. During the cruise seven points of intersection were possible to reach within a radius of 150 km. Thereof six radiosonde could be launched. The results of the comparison show a correlation between the Rayleigh$_{clear}$ and the radiosonde wind measurements of 92.8%, having a positive bias of 1.77 ms^{-1}. Without the bias correction the main deviation between Aeolus and radiosondes measurements is within 7 ms^{-1}. Excluding one non representative comparison, the Mie$_{cloudy}$ measurements correlate with 91.5%, having a positive bias of 0.52 ms^{-1}. The Aeolus wind deviations to the radiosonde profiles are all less than 6 ms^{-1}. The highest source of uncertainty in this validation is the horizontal distance between the radiosonde and Aeolus position and the low horizontal and vertical resolution of Aeolus, whereas the radiosonde measures only at one place. Nevertheless, the results agree well with observations presented at the Aeolus CAL/VAL workshop [22], having a calculated global positive bias between $<$1 ms^{-1} to 3.3 ms^{-1}, that differs in dependence of latitude, orbit phase, observation period, and Mie or Rayleigh profiles.
For the aerosol product only two comparisons were possible during the cruise. In both, the

aerosol layer is detected by Aeolus, but the particle extinction coefficient and the lidar ratio are very noisy and have only few measurements with high error bars. With these results no specific characterization of the layers is possible. For this, further validations of the aerosol product need to be done, using ground-based stations ideally in dust areas with homogeneous aerosol layers, which have a vertical range of several kilometres, to have good comparison conditions. But it has been already shown and discussed on the Aeolus CAL/VAL workshop [22], that the aerosol products lack still of a quality flag and is not yet perfectly developed.
Besides the shipborne validation, this thesis is considering land-based measurements in Leipzig. As Aeolus is passes Leipzig every Friday evening, radiosondes were launched since mid May 2019. Due to a strong decrease in emitting laser energy, the Aeolus team switched to the second laser on 16 June 2019. As after the switch a downtime of the instrument of several weeks occurred, only the five measurements before that switch are taken into account for the comparisons. The land-based validation shows much larger deviations up to more than 15 ms^{-1} and a higher error estimation, close to the limit of 8 ms^{-1}, that was defined as the error threshold for the Aeolus Rayleigh measurements in this thesis. The $\text{Rayleigh}_{\text{clear}}$ measurement correlate only with 78.1%, having a negative bias of -4.36 ms^{-1}. According to the internal weekly quality reports for the CAL/VAL teams, a negative bias was also observed in the ECMWF model comparison for the Northern Hemisphere for the time period of the land-based validation, appearing after the update of the processing chain on 16 May 2019. The reasons for the stronger deviation in the land-based validation is presumably a combination of: the increase of solar background in the Northern Hemisphere and of hot pixels associated noise, as well as the decrease in laser energy. And last but not least, some measurements recorded wind with strong southerly/northerly components, which means wind velocities close to 0 ms^{-1} along the LOS. This is lowering the correlation by having the same statistical and random errors as with high wind velocity.
The main challenges of the Aeolus mission are the occurrence of hot pixels, varying wind measurement biases, the laser energy development, and the lower atmospheric return signal. In the summary of the Aeolus CAL/VAL workshop [22] the $\text{Mie}_{\text{cloudy}}$ random error was estimated to be $\approx$ 2.5 ms^{-1}, which agrees with the mission requirements, that are between 1 ms^{-1} and 3 ms^{-1} for the precision of the HLOS components. Whereas the problems result in a larger $\text{Rayleigh}_{\text{clear}}$ random error ($\approx$ 4 ms^{-1}). Both estimated errors vary with time, especially increasing before the laser was switched, due to the low emitting laser energy. Nevertheless, analyses presented at the Aeolus CAL/VAL workshop [22], could show a significant impact of the Aeolus measurements on the NWP model forecasts,. Especially in areas with a low cover in direct wind observing systems, like in the tropical upper troposphere and the Southern Hemisphere. The analyses showed also that the impact is comparable to other in-orbit satellite observing systems.

In sum the shipborne and land-based validation is successful. It shows unique validation measurements across the Atlantic Ocean, which is a necessary contribution to the - until now - mainly model-based validations in that region. It also points out the change of quality compared to the later performed land-based validation. Having radiosonde launches before and after the laser switch, the impact of the higher laser energy on the measurements can be studied in further investigations.
Last but not least, one has to mention that the Aeolus products will be continuously improved and several reprocessing steps of the existing data will take place in the future. The obtained and analysed data set resulting from this Master thesis can be used to analyse the performance of the new generation of Aeolus products.

Bibliography

[1] https://www.esa.int/Our_Activities/Observing_the_Earth/Aeolus/Introducing_Aeolus, (visited on 24.10.2019).

[2] https://www.ecmwf.int/en/about/media-centre/science-blog/2018/improving-forecasts-new-wind-data-esas-aeolus-mission, (visited on 24.10.2019).

[3] https://www.tropos.de/en/research/projects-infrastructures-technology/coordinated-observations-and-networks/oceanet/, (visited on 01.03.2019).

[4] A. Macke et al. Radiative effects of the cloudy atmosphere from ground and satellite based observations. *EPJ Web of Conferences*, 9:83–94, 2010.

[5] T. Kanitz et al. Radiative effect of aerosols above the northern and southern Atlantic Ocean as determined from shipborne lidar observations. *Journal of Geophysical Research: Atmospheres*, 118(22):12,556–12,565, 2013.

[6] F. Rittmeister et al. Profiling of Saharan dust from the Caribbean to western Africa - Part 1: Layering structures and optical properties from shipborne polarization/Raman lidar observations. *Atmospheric Chemistry and Physics*, 17:12963–12983, 2017.

[7] Alfred-Wegener-Institut Helmholtz-Zentrum für Polar-und Meeresforschung. Polar Research and Supply Vessel POLARSTERN Operated by the Alfred-Wegener-Institut Helmholtz-Zentrum für Polar- und Meeresforschung. *Journal of large-scale research facilities*, 3, A119, 2017.

[8] W. Weischet and W. Endlicher. Einführung in die Allgemeine Klimatologie. *Borntraeger*, 2018.

[9] http://www.esa.int/spaceinimages/Missions/Aeolus, (visited on 24.10.2019).

[10] R. Engelmann et al. The automated multiwavelength Raman polarization and water-vapor lidar Polly^{XT}: the neXT generation. *Atmospheric Measurement Techniques*, 9(4):1767–1784, 2016.

[11] Holger Schmithüsen. Radiosonde measurements during POLARSTERN cruise PS116. https://doi.org/10.1594/PANGAEA.903888, *PANGAEA*, 2019.

[12] P. Ingmann and A.G. Straume. ADM-Aeolus Mission Requirements Document, AE-RP-ESA-SY-001 EOP-SM/2047. V.2:57pp, 2016.

[13] H. Pierre et al. ADM-Aeolus L2A Algorithm Theoretical Baseline Document, Particle spin-off products, AE-TN-IPSL-GS-001. V.5.5:83pp, 2017.

[14] O. Reitebuch, D. Huber, and I. Nikolaus. Alogrithm Theoretical Basis Document ATBD: ADM-Aeolus Level 1B Products, AE-RP-DLR-L1B-001. V.4.3:115pp, 2017.

[15] `https://earth.esa.int/documents/700255/3422283/day_1_12_40_rennie5eee.pdf`, (visited on 26.09.2019).

[16] C. Weitkamp. Lidar: range-resolved optical remote sensing of the atmosphere. *Springer*, 2005.

[17] D. Müller et al. Aerosol-type-dependent lidar ratios observed with Raman lidar. *Journal of Geophysical Research: Atmospheres*, 112(D16), 2007.

[18] J. Klett. Stable analytical inversion solution for processing lidar returns. *Appl. Opt.*, 20(2):211–220, 1981.

[19] A. Ansmann et al. Independent measurement of extinction and backscatter profiles in cirrus clouds by using a combined Raman elastic-backscatter lidar. *Appl. Opt.*, 31(33):7113–7131, 1992.

[20] S. Shipley et al. High spectral resolution lidar to measure optical scattering properties of atmospheric aerosols. 1: Theory and instrumentation. *Appl. Opt.*, 22(23):3716–3724, 1983.

[21] B.M. Gentry, H. Chen, and S.X. Li. Wind measurements with 355-nm molecular Doppler lidar. *Opt. Lett.*, 25(17):1231–1233, 2000.

[22] `https://nikal.eventsair.com/QuickEventWebsitePortal/aeolus-calval-and-science-workshop-2019/aeolus`, (visited on 07.10.2019).

[23] J. de Kloe et al. ADM-Aeolus Level-2B/2C Processor Input/Output Data Definitions Interface Control Document, AE-IF-ECMWF-L2BP-001. 2016.

[24] D. Tan et al. Aeolus Level-2B Algorithm Theoretical Basis Document (Mathematical Description of the Aeolus Level-2B Processor), AE-TN-ECMWF-L2BP-0023. 2017.

[25] H. Baars et al. Target categorization of aerosol and clouds by continuous multiwavelength-polarization lidar measurements. *Atmospheric Measurement Techniques*, 10(9):3175–3201, 2017.

[26] P. Seifert et al. Saharan dust and heterogeneous ice formation: Eleven years of cloud observations at a central-european earlinet site. *J. Geophys. Res.*, 115:D20201, 2010.

[27] `https://www.vaisala.com/sites/default/files/documents/RS41-SGP-Datasheet-B211444EN.pdf`, (visited on 20.10.2019).

[28] R. J. Dirksen et al. Reference quality upper-air measurements: GRUAN data processing for the Vaisala RS92 radiosonde. *Atmospheric Measurement Techniques*, 7(12):4463–4490, 2014.

[29] `https://www.vaisala.com/sites/default/files/documents/RS92SGP-Datasheet-B210358EN-F-LOW.pdf`, (visited on 20.10.2019).

[30] M. P. Jensen et al. Comparison of Vaisala radiosondes RS41 and RS92 at the ARM Southern Great Plains site. *Atmospheric Measurement Techniques (Online)*, 9(7), 7 2016.

[31] P. Hupfer and W. Kuttler. Witterung und Klima - Eine Einführung in die Meteorologie und Klimatologie. *Teubner Verlag*, 2006.

[32] `https://aeolus.services/`, (visited on 27.09.2019).

[33] `http://forecast.uoa.gr/dustindx.php?domain=atl`, (visited on 10.10.2019).

[34] G. Kallos et al. Transatlantic Saharan dust transport: Model simulation and results. *Journal of Geophysical Research: Atmospheres (1984–2012)*, 111(D9), 5 2006.

[35] D. Huber, A. Dabas, and V. Lever. ADM-Aeolus Level-2A Processor Input/Output Data Definition, AE-IF-DLR-L2A-004. 2018.

[36] H. Baars et al. An overview of the first decade of Polly$^{\mathrm{NET}}$: an emerging network of automated Raman-polarization lidars for continuous aerosol profiling. *Atmospheric Chemistry and Physics*, 16(8):5111–5137, 2016.

[37] `https://www.vaisala.com/de/products/systems/mw41`, (visited on 20.10.2019).

Disclaimer and Acknowledgement:
The presented work includes preliminary data (not fully calibrated/validated and not yet publically released) of the Aeolus mission that is part of the European Space Agency (ESA) Earth Explorer Program. Further data quality improvements, including in particular a significant product bias reduction, will be achieved before the public data release. The analysis has been performed in the frame of the Aeolus Scientific Calibration & Validation Team (ACVT), the Aeolus Data Innovation and Science Cluster (Aeolus DISC) and/or the Aeolus Science and Product quality Working Group (SAG).

Acronyms

ACCD	Accumulation Charge Coupled Device
ACVT	Aeolus Scientific Calibration & Validation Team
ADM	Atmospheric Dynamics Mission
Aeolus DISC	Aeolus Data Innovation and Science Cluster
AISP	Annotated Instrument Source Packet
ALADIN	Atmospheric Laser Doppler Instrument
AMV	Atmospheric Motion Vectors
DFU-M	Detection Front-End Unit Mie
DFU-R	Detection Front-End Unit Rayleigh
DLR	Deutsche Luft- und Raumfahrt
DWD	Deutscher Wetterdienst
CAL/VAL	calibration and validation
ECMWF	European Centre of Medium-Range Weather Forecasts
ESA	European Space Agency
EVAA	Experimental Validation and Assimilation of Aeolus observations
FFM	Flip-Flop Mechanism
FWHM	Full Width at Half Maximum
GCOS	Global Climate Obsvering System
GRUAN	GCOS Reference Upper-Air Network
HLOS	horizontal line-of-sight
HSR	High Spectral Resolution
HWP	half-wave plate
IFF	interference filter
IOCV	In orbit commissioning and validation
IR	infrared
ITCZ	Inter-Tropical Convergence Zone
LCM	laser chopper mechanism
lidar	Light detection and ranging
LOS	line-of-sight
MCA	Mie channel algorithm
MSP	Mie spectrometer

MIM	Meteorological Institute of the Ludwig Maximilian University of Munich
NWP	Numerical Weather Prediction
O–B	Observation minus Background
OBA	Optical Bench Assembly
OCEANET	A project of the German Leibniz Programme [4]
PBL	Planetary Boundary Layer
PLH	Power Laser Heads
Pol	polarising beam splitter
QWP	quarter-wave plate
RLH	Reference Laser Head
RSP	Rayleigh spectrometer
SAG	Aeolus Science and Product quality Working Group
SCA	Standard Correct Algorithm
TRO	Transmit-Receive Optics
TROPOS	Leibniz Institute for Tropospheric Research
USR	useful spectral range
UV	ultra violet

Selbständigkeitserklärung

Ich versichere hiermit, dass ich die vorliegende Arbeit selbständig verfasst und keine anderen als die angegebenen Quellen und Hilfsmittel benutzt habe.
Alle Stellen, die wörtlich oder sinngemäß aus veröffentlichten oder noch nicht veröffentlichten Quellen entnommen sind, sind als solche kenntlich gemacht.
Die Zeichnungen oder Abbildungen in dieser Arbeit sind von mir selbst erstellt worden oder mit einem entsprechenden Quellennachweis versehen.
Diese Arbeit ist in gleicher oder ähnlicher Form noch bei keiner anderen Prüfungsbehörde eingereicht worden.

Leipzig, den 24. Oktober 2019

Alina Herzog